Gondwana Research 37 (2016) 53–70

Contents lists available at ScienceDirect

Gondwana Research

journal homepage: www.elsevier.com/locate/gr

Regimes of subduction and lithospheric dynamics in the Precambrian: 3D thermomechanical modelling

R. Fischer *, T. Gerya

Geophysical Fluid Dynamics Group, Institute of Geophysics, Department of Earth Sciences, Swiss Federal Institute of Technology (ETH-Zurich), Sonneggstrasse, 5, 8092 Zurich, Switzerland

ARTICLE INFO

Article history:
Received 30 June 2015
Received in revised form 7 June 2016
Accepted 8 June 2016
Available online 21 June 2016

Handling Editor: A.R.A. Aitken

Keywords:
Precambrian
Archean
Subduction
Plate tectonics
Plume-lid tectonics

ABSTRACT

Comparing the early Earth to the present day, geological–geochemical evidence points towards higher mantle potential temperature and a different type of tectonics. In order to investigate possible changes in Precambrian tectonic styles, we conduct 3D high-resolution petrological–thermomechanical numerical modelling experiments for oceanic plate subduction under an active continental margin at a wide range of mantle potential temperature T_P ($\Delta T_P = 0 - 250$ K, compared to present day conditions). At present day mantle temperatures ($\Delta T_P = 0$ K), results of numerical experiments correspond to modern-style subduction, whereas at higher temperature conditions important systematic changes in the styles of both lithospheric deformation and mantle convection occur. For $\Delta T_P = 50 - 100$ K a regime of dripping subduction emerges which is still very similar to present day subduction but is characterised by frequent dripping from the slab tip and a loss of coherence of the slab, which suggests a close relationship between dripping subduction and episodic subduction. At further increasing $\Delta T_P = 150 - 200$ K dripping subduction is observed together with unstable dripping lithosphere, which corresponds to a transitional regime. For $\Delta T_P = 250$ K, presumably equivalent to early Archean, the dominating tectonic style is characterised by small-scale mantle convection, unstable dripping lithosphere, thick basaltic crust and small plates. Even though the initial setup is still defined by present day subduction, this final regime shows many characteristics of plume-lid tectonics. Transition between the two end-members, plume-lid tectonics and plate tectonics, happens gradually and at intermediate temperatures elements of both tectonic regimes are present. We conclude, therefore, that most likely no abrupt geodynamic regime transition point can be specified in the Earth's history and its global geodynamic regime gradually evolved over time from plume-lid tectonics into modern style plate tectonics.

1. Introduction

The accretion of Earth from matter previously dispersed in the solar nebula and subsequent impact events, among them the moon forming event (e.g. Canup, 2004), added tremendous amount of energy to the early Earth (Jaupart et al., 2007). Other important heat sources were the core–mantle differentiation and a high amount of radiogenic elements like U, Th and K (Wasserburg et al., 1964). Characteristic mantle temperatures at that time were between 50 − 300 K higher than present day conditions (Abbott et al., 1994, and references therein).

This leads to a period of a fully molten mantle, the magma ocean, which started to crystallise while the Earth was cooling. During this continuous process of cooling the crust was formed and the mantle solidified and started to convect by solid state creep. At some point during further cooling subduction processes and global plate tectonics must have initiated. However, this early subduction probably looked very different from what is called subduction today mainly due to the high mantle temperature (e.g. van Hunen and van den Berg, 2008; Sizova et al., 2010, and references therein). With the continued cooling of the Earth's mantle, also amplified by the onset of plate tectonics, the style of subduction changed throughout the Precambrian and until the present day to the modern style of subduction which is most well-known and commonly referred to as subduction.

Present day Earth allows us to not only study directly accessible data at its surface by various means but also sample geophysical data in its interior. This gives us a good understanding of the modern day geodynamic processes. However, in the study of Precambrian geodynamics natural data are much more restricted since no geophysical information for the deep Earth's interior at that time is available Gerya (2014). The only accessible data is geological, geochemical, petrological and geochronological data of Precambrian rocks from the Earth's surface. But the Precambrian rock record is relatively scarce and becomes more restricted with increasing rock age.

Major outcrops of Precambrian rocks are mainly found in cratons and continental shields. Examples of Archean outcrops are the Slave province in Canada (Bleeker et al., 1999), the Pilbara craton in Australia (Collins et al., 1998; Hickman, 2004; Van Kranendonk et al., 2004) or the Kaapvaal craton in South Africa.

Granite-greenstone terrains (GGT) are a general structural element in cratons. Greenstones form circular networks (Van Kranendonk et al.,

* Corresponding author.
E-mail address: ria.fischer@erdw.ethz.ch (R. Fischer).

http://dx.doi.org/10.1016/j.gr.2016.06.002
1342-937X/

2004) or winding belts of tholeiitic basalts and komatiites often accompanied by metasediments and banded iron formations (Bleeker et al., 1999).

For most cratons a felsic basement comprised of tonalite–trondhjemite–granodiorite (TTG) has been shown (e.g. Slave province: Bleeker et al. (1999), Pilbara craton: Van Kranendonk et al. (2004), Kaapvaal craton: Kisters and Anhaeusser (1995); Van Kranendonk (2011)). This basement usually shows a characteristic dome-and-keel structure with large TTG domes intruding into the overlaying greenstone cover (Hamilton, 1998; Van Kranendonk et al., 2004; François et al., 2014). Often several generations of granitoid intrusion can be found, sometimes within one dome with the oldest suit on the outside (Van Kranendonk et al., 2004). Several different mechanisms have been proposed to generate these patterns. Many authors discuss the similarities of greenstone belts to modern ophiolite zones both structurally (de Wit, 1998) and chemically (Furnes et al., 2015). This leads to the conclusion that plate tectonics and with it subduction might have been already operable in the Eoarchean or even Hadean (Furnes et al., 2015). Another possibility is the formation of the TTG domes by diapirism or sagduction (e.g. Hill et al., 1991; Vlaar et al., 1994; François et al., 2014). The layering of mafic greenstones on top of felsic TTGs creates a density instability which results in partial convective overturn (Collins et al., 1998; Van Kranendonk, 2011). The typical pattern of TTG domes with greenstone belts in between emerges which is best conserved in the East Pilbara (François et al., 2014). The process of sagduction does not necessarily require active plate tectonics and can therefore be seen as an alternative to an early onset of the subduction process (Hamilton, 1998).

In this context the two questions which are most strongly debated are (1) the timing and mechanism of onset of subduction and (2) the change of style in subduction throughout the Earth history. To answer these important questions, numerical geodynamic models should be used in addition to restricted natural data (e.g. Vlaar et al., 1994; van Hunen and van den Berg, 2008; Sizova et al., 2010; Gerya, 2014; Gerya et al., 2015, and references therein).

Previous studies focused on 2D numerical models of Precambrian subduction. Van Hunen and van den Berg (2008) found in particular that an increase of 200 − 300 K in the mantle potential temperature T_P leads to episodic subduction interrupted by frequent slab break-off. Sizova et al. (2010) were able to identify several geodynamic regimes mainly depending on mantle potential temperature. They found a transition from 'no-subduction' to 'pre-subduction' for a mantle 200 − 250 K hotter, where 'pre-subduction' is characterised by shallow underthrusting and two-sided lithospheric downwellings. A second transition from 'pre-subduction' to present day subduction was found at 160 − 175 K increased mantle potential temperature.

Despite the fact that Precambrian crustal deformation processes are typically characterised by three-dimensional mass redistribution (Chardon et al., 2009; Perchuk and Gerya, 2011; François et al., 2014), no 3D numerical modelling studies of Precambrian tectonics have been done so far. This study will therefore be the first to present 3D numerical modelling results. In the following, mantle temperature is identified as the dominant parameter (among others van Hunen and van den Berg, 2008; Sizova et al., 2010, 2014) which influences the subduction style. Subduction stability is then analysed back in geological time by means of exploring higher mantle potential temperature (van Hunen and van den Berg, 2008; Sizova et al., 2010, 2014), although no direct time–temperature correlation is explored in our study.

2. Methods

2.1. Model design

2.1.1. Initial and boundary conditions

To simulate the process of subduction of an oceanic plate beneath an overriding continent, a model setup (see Fig. 2a) with a size of 1000 × 328 × 680 km has been chosen. The model resolution is 2 × 2 × 2 km per cell with a subgrid resolution of 1 km for the material properties defined on Lagrangian markers. The model setup follows closely the 2D models described by Sizova et al. (2010) as well as 3D laterally variable modern subduction/collision models explored by Duretz et al. (2014) for comparison with previous results. The continental crust of the overriding plate at the left model boundary has a length of 400 km while the oceanic crust of the subducting plate has a length of 600 km on one half of the model domain and a length of 500 km in the other half to allow space for a continental corner of 100 km by 500 km at the right model boundary (Fig. 2a).

The models have been carried out with the 3D numerical I3ELVIS code (Gerya and Yuen, 2007) which is based on a conservative finite difference method with a multigrid solver and a non-diffusive marker-in-cell technique to simulate multiphase flow (Gerya and Yuen, 2003, 2007). Additionally, the 3D code also features melting of crustal and mantle rocks and volcanic addition of primordial crust from silicate melt, eclogitic phase changes as well as hydration and dehydration (Zhu et al., 2013).

The oceanic crust is modelled by a 3 km thick layer of basalt above a 5 km thick layer of gabbro. The continental crust consists of felsic rock of 35 km thickness in total while the upper continental crust is 12 km thick and the lower continental crust is 23 km thick. A lithospheric mantle of dry peridotite goes down to a depth of 90 km.

An inclined weak fracture zone of wet olivine rheology (Ranalli, 1995) is introduced which will allow focused subduction initiation at a prescribed narrow zone along the continental margin. The weak zone extends to the bottom of the lithosphere forming a straight line between continental and oceanic plate going through the entire model domain (Duretz et al., 2014).

All mechanical boundary conditions are free slip except for the bottom boundary which is open. The uppermost 12 − 15 km of the model domain are filled with 'sticky air' which acts as an internal free surface boundary condition (Crameri et al., 2012). In the uppermost 130 km constant convergence velocity conditions are applied at the left and right model boundary (except for model *A*0, where velocity boundary conditions are applied over the entire left and right model boundaries, see Fig. 3a) giving an overall convergence rate of 3.0 cm/yr partitioned as 1.0 cm/yr and 2.0 cm/yr between the left and right plate, respectively (Figs. 1 and 3b). This forced convergence rate decreases linearly to zero between 20 and 25 Myr and is set to zero after 25 Myr. These boundary conditions allow the development of a self-consistent subduction zone which will go into a retreating mode after the forced convergence is stopped and leads to extension of the overriding plate.

A simplified and instantaneous erosion and sedimentation model is implemented. Rock markers of any type which are found above the erosion level $y_{erosLev}$ are eroded instantaneously and converted to air while water markers below the sedimentation level $y_{sedilev}$ are deposited instantaneously and converted to layered sediments. The sea level $y_{waterlev}$ is held constant at a certain vertical coordinate (3 km above the initial oceanic crust level).

The temperature structure of the oceanic plate is given by the oceanic geotherm which is calculated for a given cooling age and mantle potential temperature (Turcotte and Schubert, 2002). The temperature structure in the continental plate is given by a linear geotherm. The surface temperature is fixed at 273 K whereas the temperature at the lithosphere-asthenosphere boundary (LAB) is given by the adopted asthenospheric geotherm. The thickness of the lithosphere and the depth of the LAB is defined thermally by the change in slope of the temperature profile. The asthenosphere has a fixed linear adiabatic temperature gradient of 0.5 K/km. However, the mantle potential temperature T_P (the theoretical intersection of the asthenospheric geotherm with the Earth's surface) is varied in different experiments to simulate early-Earth-like conditions ($\Delta T_P = 0 - 250$ K compared to present day reference mantle potential temperature $T_P = T_{initial} =$ 1556 K (Herzberg et al., 2007)).

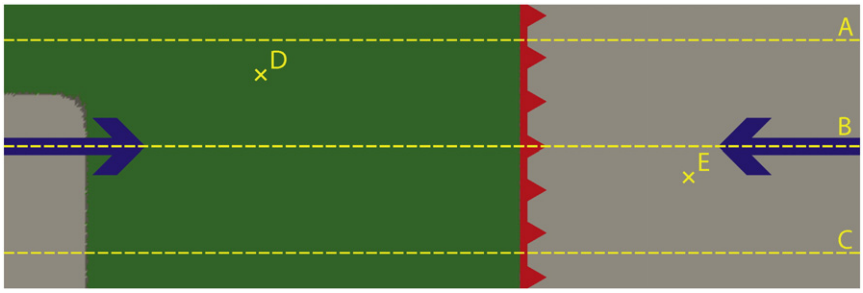

Fig. 1. Top view of the model setup used. Blue arrows indicate the direction of compression, while the red line indicates the position of the prescribed weak zone. Letters denote positions of different 2D (A)-(C) and 1D (D), (E) profiles.

2.1.2. Modelling of dehydration, hydration and water transport

The slab dehydration and mantle hydration model is based on the water markers approach (Gerya and Meilick, 2011). The equilibrium mineralogical water content is computed for the crust and the mantle as a function of pressure and temperature from thermodynamic data by free energy minimisation (Connolly, 2005; Gerya and Meilick, 2011). In addition, water is present as pore fluid with concentrations of up to 2 wt.% in the upper oceanic crust (basalt). The pore water content $X_{H_2O}(P)$ (wt.%) decreases linearly from the maximal value of $X_{H_2O}(P_0)=2$ wt.% at the surface to 0 wt.% at 75 km depth:

$$X_{H_2O}(P) = (1-0.013\cdot\Delta y)\cdot X_{H_2O}(P_0), \tag{1}$$

where y is depth (0 − 75 km). The pore water release also mimics effects of low-temperature (T<573 K) reactions, which are not included in the thermodynamic database (Gerya and Meilick, 2011). The oceanic crust dehydrates as it sinks. The timing of H_2O release by dehydration reactions is determined by the physicochemical conditions of the model and the assumption of thermodynamic equilibrium. Water propagates upward into the mantle wedge. Water propagation is modelled in the form of water markers: dehydration reactions lead to a release of water, the amount of which is stored in a newly generated water marker. Water markers move through the rocks with the following velocity:

$$v_{x,water} = v_x, \tag{2a}$$

$$v_{y,water} = v_y - v_{y,percolation} \tag{2b}$$

v_x and v_y describe the local velocity of the mantle and $v_{y,percolation}$ indicates the relative velocity of upward percolation ($v_{y,percolation}=10$ cm/yr in our experiments) (Gerya and Meilick, 2011). The water marker releases its water as soon as it encounters a rock capable of absorbing water by hydration or melting reactions at given P–T-conditions and rock composition (Gerya and Meilick, 2011).

2.1.3. Modelling of melting and crustal growth

In order to account for changes in melting conditions (e.g., solidus and liquidus temperatures — $T_{solidus}$ and $T_{liquidus}$) with varying rock composition four different melting models are used. For sediments and felsic rocks like dry or hydrated upper continental crust a granite melting model is applied (Johannes, 1985; Poli and Schmidt, 2002; Gerya et al., 2006):

$$T_{solidus} = \begin{cases} 889 + \dfrac{17900}{P+54} + \dfrac{20200}{(P+54)^2} & \text{at } P < 1200 \text{ MPa} \\ 831 + 0.06\cdot P & \text{at } P \geq 1200 \text{ MPa} \end{cases} \tag{3a}$$

$$T_{liquidus} = 1262 + 0.09\cdot P \tag{3b}$$

For all hydrated mafic rocks like upper oceanic crust, hydrated lower continental crust and new formed volcanic rocks a basalt melting model is applied (Hess, 1989; Schmidt and Poli, 1998; Gerya et al., 2006):

$$T_{solidus} = \begin{cases} 973 + \dfrac{70400}{P+354} + \dfrac{77800000}{(P+354)^2} & \text{at } P < 1600 \text{ MPa} \\ 935 + 3.5\times10^{-3}\cdot P + 6.2\cdot10^{-6}\cdot P^2 & \text{at } P \geq 1600 \text{ MPa} \end{cases} \tag{4a}$$

$$T_{liquidus} = 1423 + 0.105\cdot P \tag{4b}$$

A gabbro melting model (Hess, 1989; Gerya et al., 2006) is applied to the lower part of both oceanic and continental crust:

$$T_{solidus} = 1327 + 0.091\cdot P \tag{5a}$$

$$T_{liquidus} = 1423 + 0.105\cdot P \tag{5b}$$

For mantle peridotite in various stages of hydration a P–T–H_2O dependent melting model of Katz et al. (2003) is applied:

$$T_{solidus} = 1359 + 0.133\cdot P - 5.1\cdot10^{-6}\cdot P^2 - 43\cdot\left(X_{H_2O}\right)^{0.75} \tag{6a}$$

$$T_{liquidus} = 2053 + 0.045\cdot P - 2.0\cdot10^{-6}\cdot P^2 - 43\cdot\left(X_{H_2O}\right)^{0.75} \tag{6b}$$

Dry mantle melting is only activated at pressures less than a maximum pressure $P_{max}=10$ GPa to avoid unrealistic results arising from the melting model extrapolation.

For all crustal lithologies, the standard melt fraction is calculated according to a simplified linear melting model (Gerya et al., 2006),

$$M_0 = \begin{cases} 0, & \text{if } T < T_{solidus} \\ \dfrac{T - T_{solidus}}{T_{liquidus} - T_{solidus}}, & \text{if } T_{solidus} < T < T_{liquidus} \\ 1, & \text{if } T > T_{liquidus} \end{cases} \tag{7}$$

where M_0 is the standard volumetric degree of melting before melt extraction. For the mantle, the non-linear melting model of Katz et al. (2003) is used to calculate M_0. In both crustal and mantle rocks, the actual amount of melt M is defined as the difference between the standard melt fraction M_0 and the amount of previously extracted melt $\sum_n M_{ext}$ which is accumulated for each marker in the course of the model where n is the number of melt extraction episodes,

$$M = M_0 - \sum\nolimits_n M_{ext} \tag{8}$$

To simulate melt extraction an extraction threshold M_{max} (see Tables S1 and 2) is defined. If the total amount of melt M on a marker surpasses this threshold (i.e. when $M>M_{max}$) all melt except for a non-extractable part M_{min} (see Tables S1 and 2) is extracted: $\sum_{n+1} M_{ext} = \sum_n M_{ext} + M - M_{min}$. The amount of extracted melt is then instantaneously transported to the surface and deposited as volcanic crust.

The eruption efficiency in these models therefore is 100%. This is a model simplification since eruption efficiency on Earth is estimated to be around 5 − 20% and thus most magmatic rocks are added to the crust as intrusions (plutons) rather than volcanic sequences (Crisp, 1984). The amount of volcanic rocks in our models will therefore be overestimated while melt emplacement into the crust in the form of intrusions will be neglected. The consequences are higher surface heat flux and larger heat loss to the atmosphere (Keller and Tackley, 2009).

Another consequence of the implemented melting and crustal growth approach is that the total volume of rock is not conserved as the depleted mantle rock will not decrease in volume in our incompressible thermomechanical model. This discrepancy is addressed by adding new 'sticky air material' at the left and right model boundary and allowing mantle to escape through the bottom of the model.

2.1.4. Density changes due to phase transitions and mantle depletion

For the basalts of the upper and lower oceanic crust a phase transition from basalt to garnet–granulite and then eclogite (Ito and Kennedy, 1971) is taken into account. Eclogitisation of subducted crust is implemented in a simplified manner as a linear density increase with pressure from 0% to 16% in the PT-region between the experimentally determined garnet-in and plagioclase-out phase transitions in basalt (Ito and Kennedy, 1971):

$$\begin{aligned} P_{Ga-In} &= \begin{cases} -9213.25 + T \cdot 15.25, & \text{if } P \geq 3000\ bar \\ 3000.0, & \text{if } P < 3000\ bar \end{cases} \\ P_{Pl-Out} &= \begin{cases} -1560 + 20 \cdot T, & \text{if } P \geq 15000\ bar \\ 15000.0, & \text{if } P < 15000\ bar \end{cases} \end{aligned} \tag{9}$$

$$\rho_e = \begin{cases} \rho_b, & P \leq P_{Ga-In} \\ \rho_b \cdot \left(1.0 + 0.16 \cdot \dfrac{P - P_{Ga-In}}{P_{Pl-Out} - P_{Ga-In}}\right), & P_{Ga-In} < P < P_{Pl-Out} \\ \rho_b \cdot 1.16, & P \geq P_{Pl-Out}, \end{cases} \tag{10}$$

where P_{Ga-In} is the temperature dependent basalt to garnet–granulite transition pressure, P_{Pl-Out} is the temperature dependent garnet–granulite to eclogite transition pressure and ρ_b and ρ_e are the basalt and eclogite densities respectively.

Depending on the accumulated amount of extracted melt $\sum_n M_{ext}$ the density of solid peridotite and solid fraction of partially molten peridotite is adjusted in the following way:

$$\rho_{s,depleted} = \rho_s \cdot (1.0 - 0.04 \cdot - \textstyle\sum_{n-1} M_{ext}) \tag{11}$$

With increasing amount of extracted melt, the density of the residue is decreasing (Schutt and Lesher, 2006). For mantle peridotite with an accumulated amount of extracted melt $\sum_n M_{ext} > 0.3$ the mantle is considered to be strongly depleted and will be visualised as lithospheric instead of asthenospheric peridotite. However further depletion is still possible.

2.1.5. Rheological model

16 different rock types (not including 'sticky air' and 'sticky water') are available in both solid and partially molten state (see Fig. 2b). To each of these rock types one of four different visco-plastic flow laws is applied. A wet quartzite flow (Ranalli, 1995) law is applied to sediments and upper crustal material. The lower crust follows a plagioclase An_{75} flow law and dry or wet mantle follow a respective (i.e., dry or wet) olivine flaw law (Ranalli, 1995) (see Table 1 for a full compilation of material properties).

A visco-plastic rheology is employed, where the relationship between the deviatoric stress σ'_{ij} and strain-rate $\dot{\epsilon}_{ij}$ is described by the visco-plastic constitutive law. For incompressible viscous deformation this results in the law of viscous friction,

$$\sigma'_{ij} = 2\eta_{eff}\dot{\epsilon}_{ij}, \tag{12}$$

where

$$\dot{\epsilon}_{ij} = \frac{1}{2}\left(\frac{\partial v_i}{\partial x_j} + \frac{\partial v_j}{\partial x_i}\right), \tag{13}$$

where η_{eff} denotes the effective viscosity, which depends on pressure, temperature, composition, strain rate and degree of melting.

For the ductile creep regime, contributions from different flow laws such as dislocation and diffusion creep are taken into account using the inverse average ductile viscosity $\eta_{ductile}$,

$$\frac{1}{\eta_{ductile}} = \frac{1}{\eta_{newt}} + \frac{1}{\eta_{powl}}, \tag{14}$$

Where η_{newt} and η_{powl} are effective viscosities for Newtonian diffusion and power-law dislocation creep, respectively, computed as

$$\eta_{newt} = \frac{1}{2} B_D \sigma_{crit}^{1-n} \exp\left(\frac{E_a + PV_a}{RT}\right), \tag{15a}$$

$$\eta_{powl} = \frac{1}{2} B_D^{\frac{1}{n}} (\dot{\epsilon}_{II})^{\frac{1-n}{n}} \exp\left(\frac{E_a + PV_a}{nRT}\right), \tag{15b}$$

where $\dot{\epsilon}_{II} = \sqrt{1/2(\dot{\epsilon}_{ij})^2}$ is the second invariant of the strain-rate tensor, E_a, V_a are activation energy and volume respectively, B_D is an experimentally defined material constant, n is the stress exponent and σ_{crit} is the diffusion–dislocation transition stress (see Table 1).

For brittle or plastic deformation, a yield stress σ_{yield} is defined, which depends on the cohesion C_0, the effective internal friction angle ϕ_{eff} and the pressure. An upper viscosity limit $\eta_{plastic}$ of the yielding material can now be calculated:

$$\sigma_{yield} = C_0 + P\sin\left(\phi_{eff}\right) \tag{16a}$$

$$\eta_{plastic} = \frac{\sigma_{yield}}{2\dot{\epsilon}_{II}}, \tag{16b}$$

In high stress regions where $\sigma_{II} > 10^8$ MPa the Peierls creep mechanism is invoked additionally (Katayama and Karato, 2008).

$$\dot{\epsilon}_{II,Peierls} = A_{Peierls}\sigma_{II}^2 \exp\left\{-\frac{E_a + PV_a}{RT}\left[1 - \left(\frac{\sigma_{II}}{\sigma_{Peierls}}\right)^k\right]^q\right\}, \tag{17a}$$

$$\eta_{Peirls} = \frac{\sigma_{II}}{2\dot{\epsilon}_{II,Peierls}}, \tag{17b}$$

where σ_{II} is the second stress invariant, $A_{Peierls} = 10^{-4.2}\mathrm{s}^{-1}\mathrm{MPa}^{-2}$ is a material constant for Peierls creep, $\sigma_{Peierls} = 9.1 \cdot 10^9$ MPa the dry Peierls stress which defines the maximum strength of the material similar to the yield stress. The two exponents $k = 1.0$ and $q = 2.0$ are influenced by limiting factors of the dislocation motion (Katayama and Karato, 2008).

The effective viscosity $\eta_{eff}(T,P,c,M)$ is now the minimum of all viscosity values,

$$\eta_{eff} = min\left\{\eta_{ductile}, \eta_{Peierls}, \eta_{plastic}\right\}. \tag{18}$$

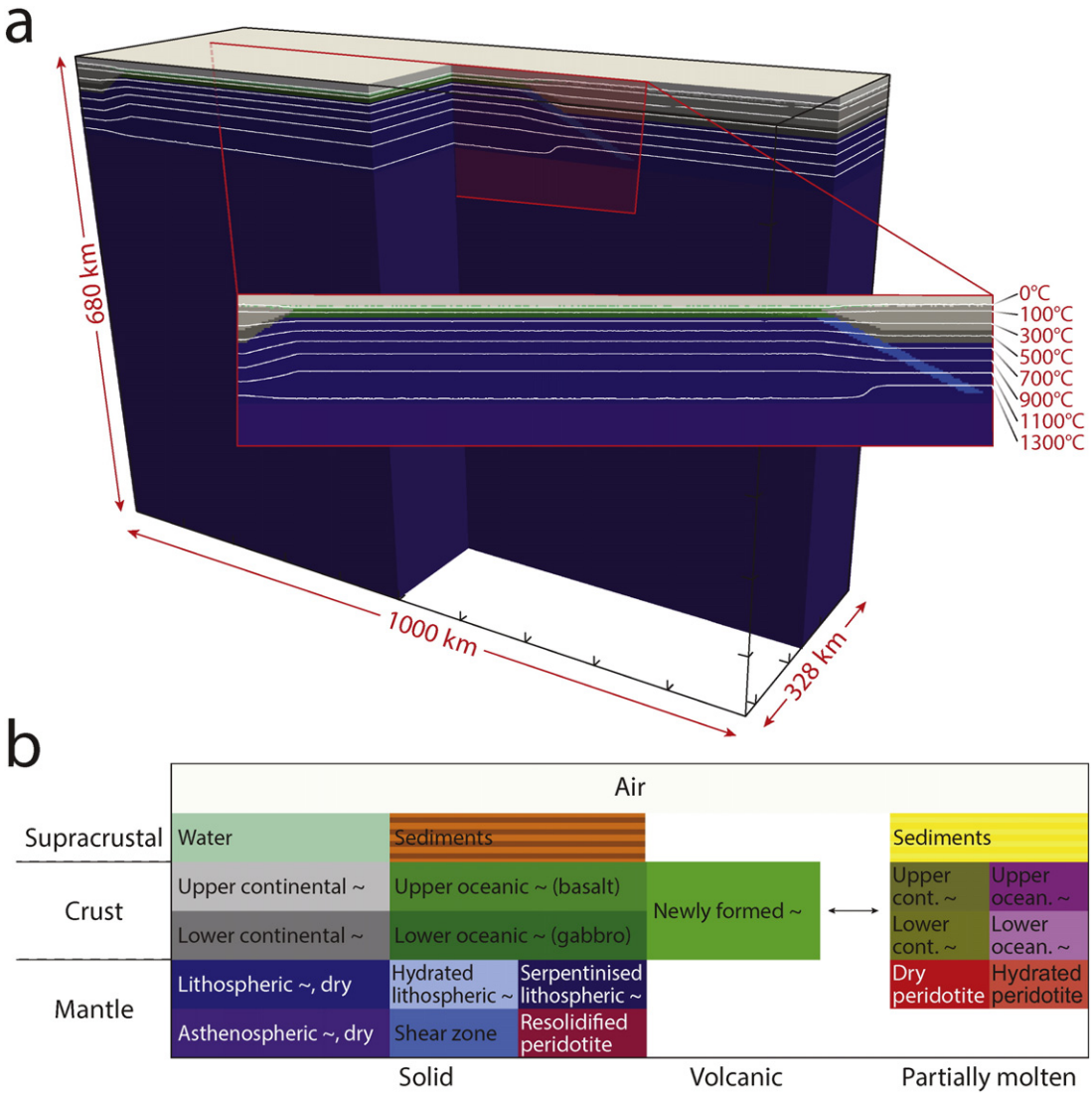

Fig. 2. (a) Initial model setup. An enlarged view of the future subduction area is shown in the inset. (b) All available material types and their colour code in both solid and partially molten state as will be used throughout this paper.

We use 10^{19} Pa·s and 10^{24} Pa·s as respectively lower and upper cut-off viscosity limits for all types of materials.

2.1.6. Governing conservation equations

Momentum, mass and heat conservation equation for 3D creeping flow all need to be satisfied simultaneously.

The conservation of momentum is described by the 3D Stokes equation with the extended Boussinesq approximation. Density is assumed to be constant except in the buoyancy force term where temperature and volatile content play an important role and density therefore varies locally as a function of temperature, pressure, composition and melt fraction:

$$\frac{\partial \sigma'_{ij}}{\partial x_j} = \frac{\partial P}{\partial x_i} - g_i \rho(T, P, c, M) \tag{19}$$

Conservation of mass is approximated by the incompressible continuity equation:

$$\nabla \cdot \vec{v} = 0. \tag{20}$$

The temperature equation satisfies the conservation of energy:

$$\rho C_p \left(\frac{DT}{Dt}\right) = -\nabla \cdot \vec{q} + H_r + H_a + H_s, \tag{21a}$$

$$H_r = \text{const. (depends on composition)}, \tag{21b}$$

$$H_a = T\alpha \vec{v} \nabla P, \tag{21c}$$

$$H_s = \sigma'_{ij} \dot{\epsilon}'_{ij}, \tag{21d}$$

where heat flux is denoted by $\vec{q} = -k(T, p, c)\nabla T$ with k being the thermal conductivity. H_r, H_a, H_s denote radiogenic, adiabatic and shear heating respectively. Latent heating is included implicitly by means of equilibrium melting/crystallisation which will change the effective heat capacity (C_{Peff}) and the effective thermal expansion (α_{eff}) (Burg and Gerya, 2005; Sizova et al., 2010) of the melting/crystallising rock as follows,

$$C_{Peff} = C_P + H_L \left(\frac{\partial M}{\partial T}\right)_{P=const}, \tag{22a}$$

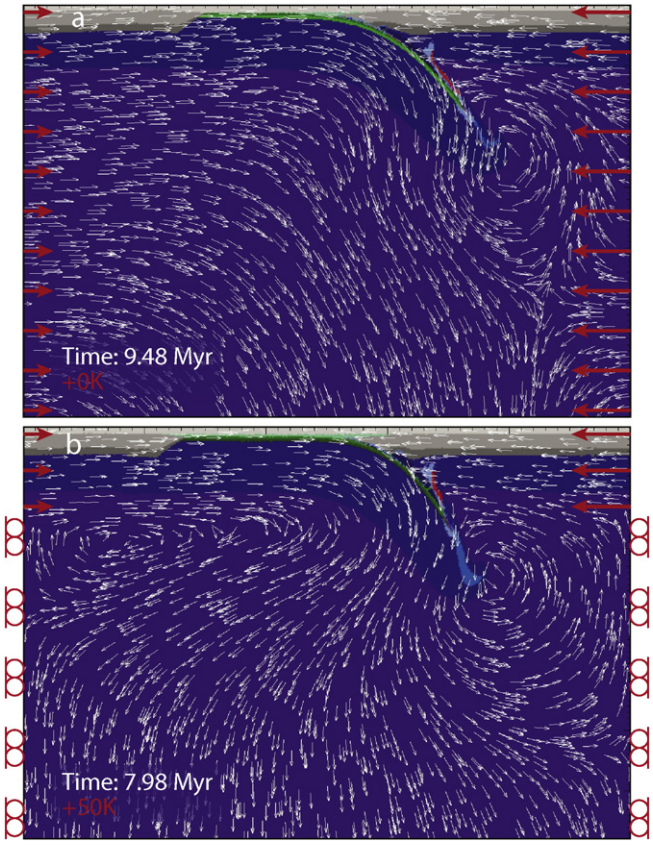

Fig. 3. Imposed side boundary conditions for models (a) *A0* and (b) *A1* to *A6*, where arrows indicate compression and wheels indicate free slip conditions. Position of the slice corresponds to profile B in Fig. 1.

$$\alpha_{\text{eff}} = \alpha + \rho \frac{H_L}{T} \left(\frac{\partial M}{\partial P} \right)_{T=const}, \tag{22b}$$

where heat capacity C_P and thermal expansion α denote properties of the solid rock.

2.2. Variations in the mantle temperature

2.2.1. Development of the mantle geotherm during Earth history

The important difference between the Precambrian and the Phanerozoic is the increased upper mantle and crustal temperature in earlier Earth history due to higher radiogenic and primordial heating rates. Reconstructions of the varying mantle potential temperature during Earth history have already been undertaken by several authors. Geochemical studies show an increase of mantle potential temperature $\Delta T_P = 200-300$ K at 3 Ga (Abbott et al., 1994; Herzberg et al., 2007, 2010, and references therein) with a spread in T_P between up- and downwelling regions of up to 200 K (McKenzie and Bickle, 1988; Abbott et al., 1994; Herzberg et al., 2007, 2010). However, no evidence is found for a sudden change in global ambient mantle potential temperature (Abbott et al., 1994; Herzberg et al., 2007, 2010, and references therein). Similar results are obtained by Labrosse and Jaupart (2007) under the assumption of a plate tectonics regime: Their 1D numerical models also show a maximum at 3 Ga but a smaller ΔT_P of 150 K.

2.2.2. Reference model series

Due to the demanding computational requirements for high-resolution 3D modelling this study will focus on the variation of mantle potential temperature ΔT_P which, according to Sizova et al. (2010), is the major reason for observed changes in geodynamic regimes through the Earth history. Mantle potential temperature is roughly correlated with time and influences other important parameters like the viscosity profile. To model subduction at different stages of Earth history, the

Table 1
Material properties[a] as well as applied rheology and melting model is listed for each of the used lithologies as given in Fig. 2b.

Material		Rheology	ρ_0	k	Melting	H_r	H_L	ϕ_{eff}	σ_{crit}	C_P
		[$MPa^{-n}s^{-1}$],[−],[kJ],[J/bar]	[kg/m^3]	[K]	[$\frac{W}{m \cdot K}$]	[$\frac{\mu W}{m^3}$]	[$\frac{kJ}{kg}$]	[−]	[MPa]	[$\frac{kJ}{kg}$]
Sediments	Solid	Wet quartzite flow law	2600	$0.64+\frac{807}{T+77}$	Eq. (3)	2.0	300	0.0	0.03	1.0
	Molten	$B_D = 1.97 \cdot 10^{17}$, $n = 2.3$,	2400						0.0	1.5
Dry felsic crust	Solid	$E_a = 154$, $V_a = 0$	2750			1.0		0.15	0.03	1.0
	Molten		2400			2.0		0.0	0.0	1.5
Hydrated felsic crust	Solid		2700			1.0			0.03	1.0
	Molten		2400						0.0	1.5
Basalt	Solid		3000	$1.18+\frac{474}{T+77}$	Eq. (4)	0.25	380		0.03	1.0
	Molten		2900						0.0	1.5
Lower continental crust	Solid	Plagioclase An_{75} flow law	2950	$1.18+\frac{474}{T+77}$	Eq. (5)	0.5	380	0.15	0.03	1.0
	Molten	$B_D = 4.80 \cdot 10^{22}$, $n = 3.2$,	2400	$0.64+\frac{807}{T+77}$		2.0		0.0	0.0	1.5
Gabbro	Solid	$E_a = 238$, $V_a = 0$	3000	$1.18+\frac{474}{T+77}$		0.25		0.6	0.03	1.0
	Molten		2900					0.0	0.0	1.5
Hydrated basalt	Solid		2900		Eq (4)	0.5			30.0	1.0
	Molten		2400	$0.64+\frac{807}{T+77}$		1.0				
Dry mantle peridotite	Solid	Dry olivine flow law	3300	$0.73+\frac{1293}{T+77}$	Eq. (6)	0.022	400	0.6	0.03	1.0
	Molten	$B_D = 3.98 \cdot 10^{16}$, $n = 3.5$,	2900					0.0	0.0	1.5
		$E_a = 532$, $V_a = 0.8$								
Hydrated mantle peridotite	Solid	Wet olivine flow law	3300	$0.73+\frac{1293}{T+77}$	Eq. (6)	0.022	400	0.0	30.0	1.0
	Molten	$B_D = 5.01 \cdot 10^{20}$, $n = 4.0$,	2900						0.0	1.5
Weak zone	Solid	$E_a = 470$, $V_a = 0.8$	3300			0.05			30.0	1.0
	Molten		2900			0.022			0.0	1.5
Serpentinite,	Solid		3300		–		–		30.0	1.0
References[b]		4, 1	1, 2	3		1	1, 2			

[a] For all rock types: Cohesion $C_0 = 1$ MPa, thermal expansion coefficient $\alpha = 3.0 \cdot 10^{-5}$ K^{-1} and compressibility $\beta = 1.0 \cdot 10^{-5}$ GPa^{-1}.
[b] (1) Turcotte and Schubert (2002), (2) Bittner and Schmeling (1995), (3) Clauser and Huenges (1995), (4) Ranalli (1995), (5) Schmidt and Poli (1998)

reference mantle potential temperature $T_{initial} = 1556$ K (Herzberg et al., 2007) in the initial models is increased by some constant value $\Delta T_P = T(t) - T_{initial}(0-250\ \text{K})$ (Fig. 4). This way the asthenospheric adiabatic thermal gradient (0.5 K/km) is kept constant, while the lithospheric geotherm flattens and leads to a weakening of the crust and the subcrustal lithospheric mantle (Fig. 4).

The reference model *A0* corresponds to a typical present day subduction setup (after Duretz et al., 2014) and has a mantle potential temperature of $T_{initial} = 1556$ K. The Precambrian models *A1* to *A6* differ from the initial model in temperature $\Delta T_P = [50,100,150,175,200,250]$ K.

2.3. Numerical constraints and setup dependencies

This model setup is constructed to satisfy present day subduction conditions. For example, the radiogenic heating is not varied between models since previous work of Sizova et al. (2010) demonstrated its rather minor influence for relatively short timescales (few Myr to few tens Myr) investigated by our numerical modelling study. To account for increased radiogenic and primordial heating in the Precambrian mantle, the mantle potential temperature T_P is increased, which also results in hotter oceanic and continental lithospheric geotherms. The model setup will therefore become less accurate with increasing ΔT_P roughly corresponding to earlier times in Earth history.

Due to the chosen type of model setup the models will go into a retreating mode of subduction in the oceanic domain (Duretz et al., 2014). After collision and further retreating the model is stopped when the trench reaches the model boundary. Models at higher ΔT_P are more challenging insofar as more melt is produced as well as higher velocities and sharper viscosity contrast are observed. A relatively large minimum viscosity of 10^{19} Pa·s and very short timesteps (<100 Myr) are necessary to stabilise these models. For the present day model *A0*, 50 Myr of model development take ~3 months of compute time which increases to ~6 months compute time for only 6.5 Myr of model development for model *A6* at the highest mantel temperature $\Delta T_P = 250$ K.

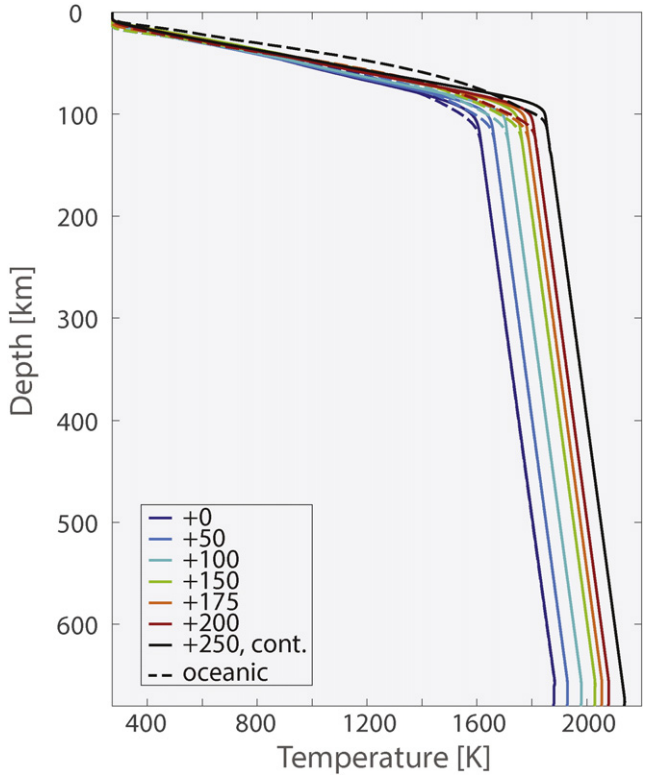

Fig. 4. Temperature profiles for the reference models (see Table 2). Solid lines indicate profiles in continental crust (Fig. 1, position E) while dashed lines indicate profiles in the oceanic crust (Fig. 1, position D).

Table 2
List of all reference models (see Section 2.1.1 for a full description). t_{max} is the maximum model time reached from the beginning of the experiment and BC are the implemented boundary conditions shown in Fig. 3.

Model	ΔT_P	M_{min}, M_{max} [wt.%]	t_{max} [Myr]	Comment Regime/Fig.	BC
A0	0	2, 4	54.17	I, Fig. 5	Fig. 3a
A1	50	2, 2	34.66	II	Fig. 3b
A2	100	2, 2	26.03	II, Fig. 6	Fig. 3b
A3	150	2, 2	22.65	II	Fig. 3b
A5	175	2, 2	23.36	III, Fig. 7	Fig. 3b
A4	200	2, 2	9.17	IV	Fig. 3b
A6	250	2, 2	6.47	IV, Fig. 8	Fig. 3b

3. Results

In the following a systematic numerical investigation of the subduction process is undertaken and its spatial and temporal variations in crustal growth, arc formation, plate thickness and dynamic regime are discussed in relation with imposed mantle potential temperature changes. An overview over the discussed models is given in Table 2 and Figs. 5 to 8 as well as Figs. S1 to S4 for melt composition.

3.1. Reference model for present day subduction ($\Delta T_P = 0$ K)

Starting from the setup as shown in Fig. 1 the model is compressed with a total convergence speed of 3 cm/yr. Subduction initiates at the prescribed weak zone and a 6 − 8 km deep trench forms (Fig. 9) which starts to fill with sediments. The subducting oceanic plate is driven below the overriding continental plate and bends downward (Fig. 5a). The overriding plate is compressed and thickened and forms a mountain range with an elevation of approximately 3 − 4 km (see Fig. S7 for the topographic evolution, where Figs. S7d and S7e correlate with the collisional stage). Scraping of the subducting upper crust (sediments and basalts) forms an accretionary wedge between the two plates (Fig. 12a). Water is transported down together with the subducting hydrated oceanic crust and hydrates both the overriding plate and the asthenospheric mantle wedge above the slab. Due to porous water release from the oceanic crust, felsic continental crust of the overriding plate becomes hydrated which leads to a drop in viscosity, and triggers formation of a subduction channel (Fig. 12b). Bound water, which is dragged down and released at greater depths, allows hydration of mantle peridotite on top of the slab. In the first 10 Myr the slab subducts at a shallow angle (Fig. 5a). From 8 Myr on the hydrated peridotite starts to partially melt and the relatively warm, advancing slab tip is slightly deflected upwards by asthenospheric flow around the subducting and steepening slab within the next 9 Myr. After ~17 Myr the slab subducts into the mantle at a steep angle of almost 90°. The whole upper surface of the slab is covered by a continuous layer of hydrated peridotite, which becomes partially molten at higher temperature conditions. Hydrated peridotite is positively buoyant compared to the ambient dry mantle and starts to rise back up along the subduction channel and penetrates lithosphere and crust of the overriding continent after ~18 Myr further hydrating lower continental crust in proximity of the slab by dehydration-released fluids (Figs. 5b and 12b).

At the same time the incoming continent which is carried by the subducting plate collides with the overriding plate and the initial oceanic basin becomes closed. Within this transitional stage (20 − 25 Myr) compression boundary conditions are gradually deactivated. The incoming continent is subducted to great depth of over 100 km before the slab breaks off under the continent-continent collision zone opening a window in the subducting plate. A Subduction-Transform Edge Propagator (STEP) (Govers and Wortel, 2005) associated with plate tear forms along the boundary between continental and oceanic domains

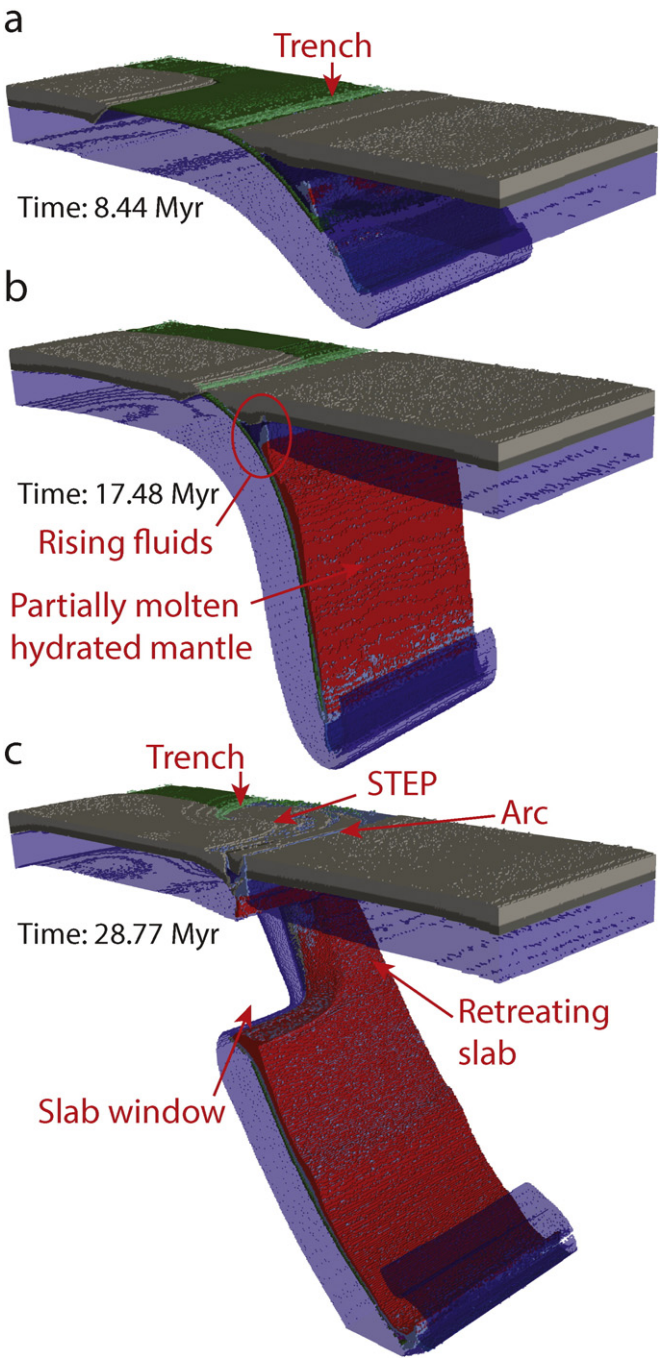

Fig. 5. Evolution of the present day reference model *A*0 at $\Delta T_P = 0$ K. The model shows an oceanic-continental subduction with the formation of a trench, (b) a magmatic arc and then continent-continent collision and (c) the opening of a slab window and the formation of a STEP boundary (see text for details and Fig. S1 for detailed melt distribution).

of the subducting plate (Fig. 5c). Subduction in the oceanic domain continues in a retreating manner after the window opening solely due to the slab-pull and the retreating trench forces the overriding plate to extend (Duretz et al., 2014).

3.2. Influence of mantle potential temperature increase ΔT_P

3.2.1. Variations in the retreating speed of the subducting slab and trench

In the presented models the applied setup and boundary conditions (see Sections 2.1.1 and 2.3) lead to the formation of a self-consistent subduction with its major driving forces being compression and slab-pull. After the collision event in the continental domain (and the subsequent shut-off of the velocity boundary conditions at 20 – 25 Myr) the only remaining driving force is slab-pull which leads to a retreat of the subducting slab and trench and to an extension of the overriding plate (Fig. 9 and Duretz et al. (2014)).

Fig. 9 shows the minimum elevation automatically picked along a surface profile in either the oceanic or continental domain of the model. In the present day model ($\Delta T_P = 0$ K, see also Fig. S7) a 6 – 8 km deep trench is formed within <5 Myr (Fig. 9a and b). In the continental domain this trench is closed again during the collisional stage (Figs. 5c and 9c). Looking at the lateral evolution the trench only migrates by a short

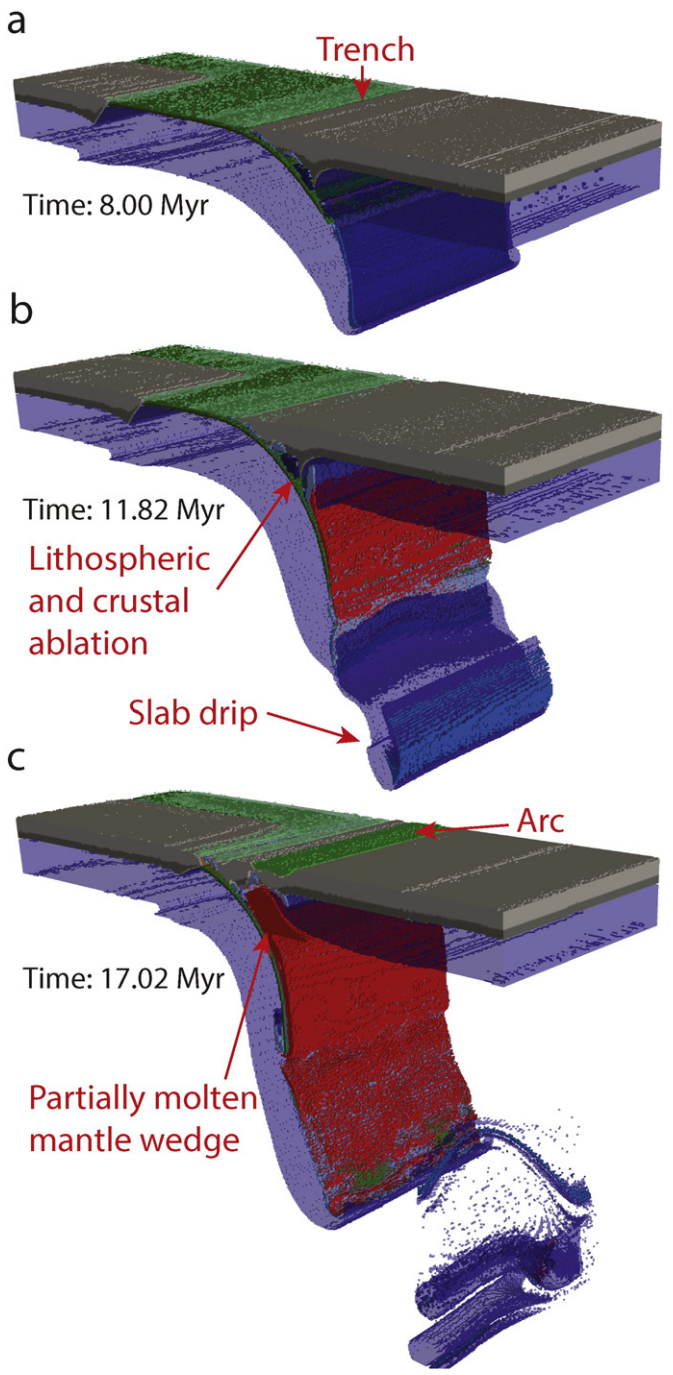

Fig. 6. Evolution of the model *A*2 at $\Delta T_P = 100$ K. The model shows (a) an irregular LAB, (b) ablative subduction and necking of the slab, (c) partial melting of the mantle wedge and a widening of the magmatic arc (see text for details and Fig. S2 for detailed melt distribution).

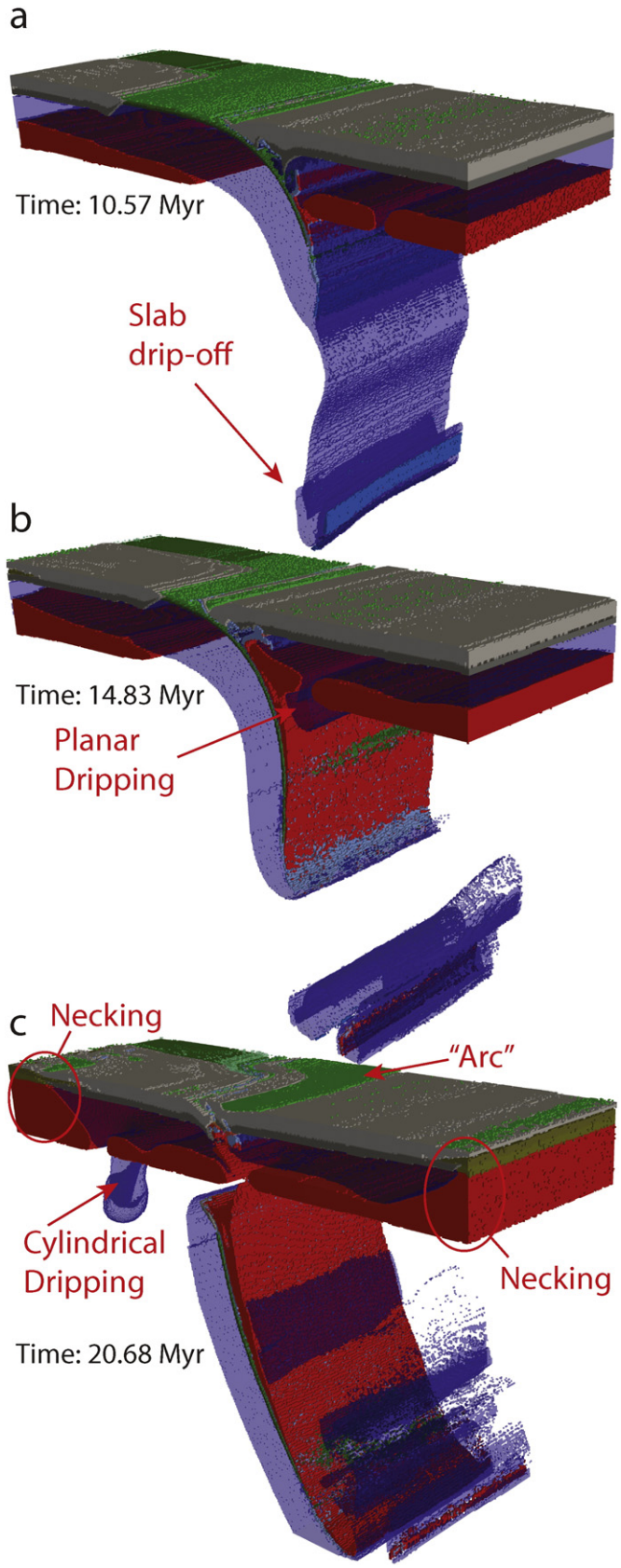

Fig. 7. Evolution of the model *A5* at $\Delta T_P = 175$ K. The model shows (a) early slab necking, (b)-(c) both planar and cylindrical off-slab lithospheric dripping (see text for details and Fig. S3 for detailed melt distribution).

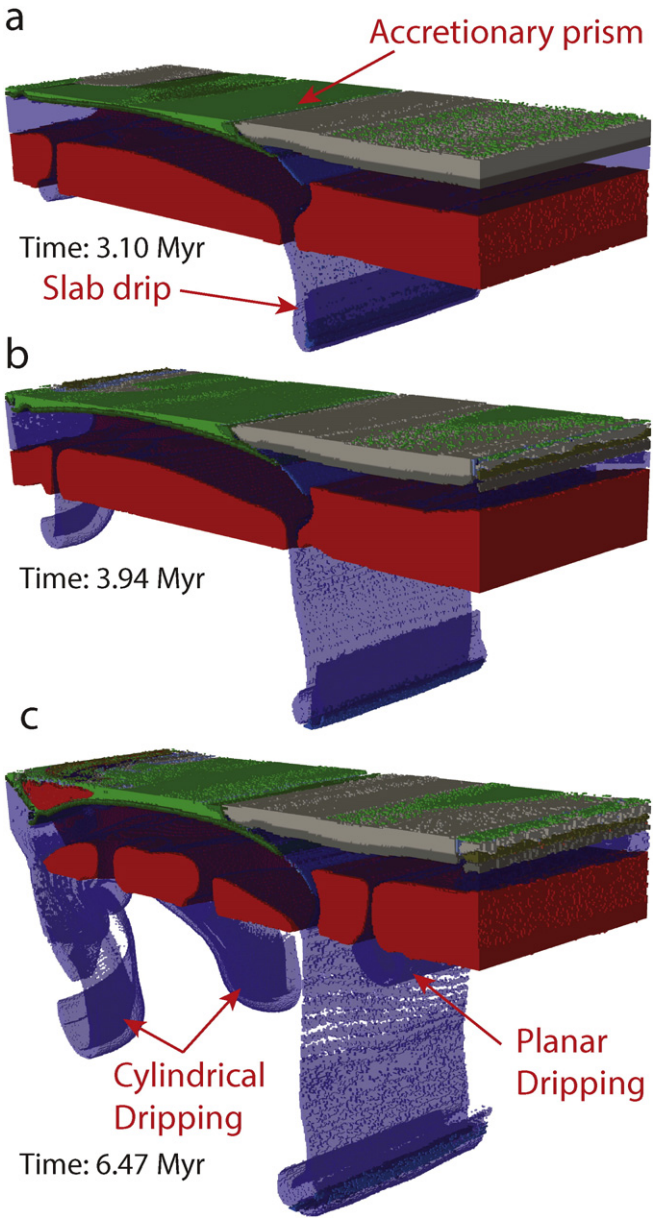

Fig. 8. Evolution of the model *A6* at $\Delta T_P = 250$ K. The model shows intense non-arc-related basaltic volcanism (light green), (a) rapid necking of the slab tip, (b)-(c) formation of very large accretionary prism (see text for details and Fig. S4 for detailed melt distribution).

distance of 50 km before the collisional stage is reached (Fig. 9d). In the oceanic domain the distance of retreat matches the one found in the continental domain up to the collisional stage. After collision the velocity of retreat is increasing and it slows down again close to the model boundary at a distance of 600 km from the original trench position (Fig. 9b).

Models for $\Delta T_P = 50 - 100$ K follow the same pattern (Figs. 9 and S8) and the collisional stage looks very similar. However, the trench in the continental domain tends to close earlier with increasing ΔT_P (Fig. 9c). The same observation can be made for the oceanic domain, where the trench retreats faster for higher ΔT_P (Fig. 9b).

Models at $\Delta T_P = 150 - 175$ K (Fig. S9) have a delayed formation of the trench in addition to the earlier closing (Fig. 9a and c). Model *A5* at $\Delta T_P = 175$ K can therefore not reach a maximum trench depth of 8 km in the continental domain (Fig. 9c). The profiles also become increasingly more erratic, which signifies that it gets increasingly more complicated to pick a definite trench.

For $\Delta T_P = 200 - 250$ K the 'trench' is above sea level for the most time (Fig. 9a and c and topographic figures in Fig. S10). The strongly

erratic jumps between 0 – 50 km and 350 – 400 km mainly visible in the continental domain of the model (Fig. 9d), hint at the formation of two 'proto'-trenches at both sides of the oceanic plate, the active and the passive margin. Similar observations are made in the alternative model *B4h* (see Table S1 and Figs. S5 and S6).

Higher ΔT_P leads to a faster retreat of the trench. The faster retreat is assisted by both a weaker mantle which allows faster slab retreat and a weaker continental crust which allows faster extension of the overriding plate. However, there is also a counteracting trend with increasing ΔT_P of decreasing trench depth, caused by stronger volcanic activity.

3.2.2. Variations in slab geometry and behaviour

In the Phanerozoic model *A0* it takes 17 Myr of subduction to reach the collisional stage (Fig. 5b and c). The slab penetrates the mantle at a steep angle of 60° – 70°. The slab tip bends slightly upward however the slab stays coherent during the entire subduction process (Figs. 5b and 10a).

At a moderate increase in mantle temperature of $\Delta T_P = 100$ K no large-scale differences are observed in the subduction process (Fig. 6). There are some minor changes however. During subduction initiation and in the early stages of subduction, parts of the overriding lithosphere are entrained and subducted as well (see Figs. 10b, 11c and 12c). The subducting plate steepens to its final near vertical angle of 80° – 90° of descent within a shorter timescale of ~11 Myr (Fig. 10b). After 11 and 13 Myr sheet-like drips develop from the relatively warm advancing slab tip (Fig. 6b and c) and after 20 Myr necking of the slab can be observed at 400 km depth (Fig. 11d).

For high upper mantle temperature $\Delta T_P = 200$ K the slab tip drips off nearly immediately after subduction initiation at 2 Myr (Fig. 12e). In the model *A4* however the slab only reaches a depth of 300 km after 9 Myr (Fig. 10c) and no weakening due to slab bending can be observed (Fig. 11e). The subduction process remains unfinished and the collisional stage is never reached. In the alternative model *B4h* (see Table S1 and Figs. S5 and S6) the slab reaches the bottom of the model domain. However shortly after subduction initiation the slab starts to lose coherence and breaks up into several pieces by necking (Figs. S5d to S5f).

For $\Delta T_P = 250$ K the slab tip drips off immediately after beginning of the simulation (Fig. 8a). Due to strongly decreased crustal and mantle viscosity, the respective model *A6* evolves very rapidly and reaches only an age of 6.5 Myr. By the end of the simulation the slab has underthrusted the overriding plate by ~160 km but only reaches a depth of 150 km, no slab bending has occurred (Figs. 8c and 10d).

Increasing ΔT_P therefore leads to an increase in subduction speed and earlier and more frequent necking of the slab, which finally results in destabilisation (breaking down) of the subduction process.

3.2.3. Variations in geometry and composition of the accretionary prism

Both geometry and composition of the accretionary prism are changing with changing ΔT_P. In the Phanerozoic model *A0* ($\Delta T_P = 0$ K) the accretionary prism consist of a growing wedge of thickened basaltic upper crust topped by a thickening sediment layer (Fig. 12a). At greater depths, the subduction channel is composed of hydrated crustal rocks and serpentinised overriding lithospheric mantle forms between the plates, thus lubricating the subduction process (Fig. 12a). With ongoing

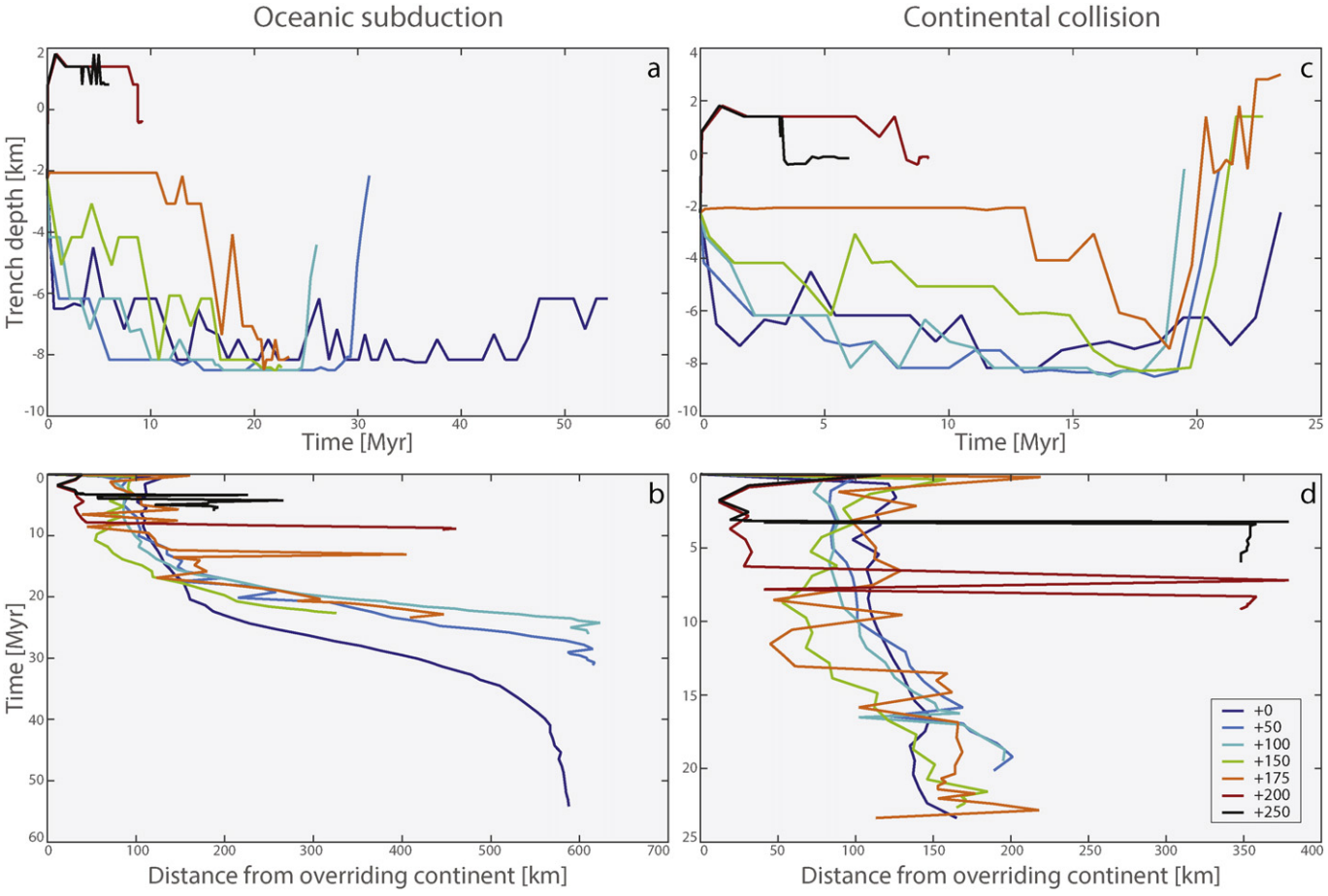

Fig. 9. Observations of trench retreat at different ΔT_P. The subduction trench is defined as the minimum of the surface profile, where oceanic subduction profiles are taken along profile A (Fig. 1) for (a) and (b) and along profile C (Fig. 1) for (c) and (d). (a) and (c) show evolution of the trench depth with time in the oceanic and continental domain respectively. (b) and (d) show the distance of retreat from the original trench position (given by the red line in Fig. 1) in the oceanic and continental domain respectively.

subduction, the size of the accretionary prism is reduced and the subduction channel is thinned (Fig. 12b).

At a small increase in $\Delta T_P = 50 - 100$ K, directly after subduction initiation the overriding plate is slightly buckled close to the wedge. This leads to the formation of a serpentinite pocket (i.e. pocket-like subduction channel) between the subducting oceanic crust and the hydrated continental crust, which is filled by serpentinised lithospheric mantle peridotite intermixed with subducted oceanic crust and hydrated continental crust (Fig. 12c). With increasing mantle potential temperature, the lower crust of the overriding plate tends to delaminate after subduction initiation, which enables the formation of larger serpentinite pockets between subducting oceanic crust and overriding continental crust. Compared to model *A0* a thick sedimentary wedge is formed during later stages of subduction which persists until the collisional stage (Fig. 12d).

For $\Delta T_P = 150 - 175$ K new crust formed by volcanic processes plays a major role in both formation and composition of the accretionary prism. In model *A5* ($\Delta T_P = 175$ K) large parts of the ocean floor are covered by mantle-derived basalts very early in the subduction process and this is reflected by the accretionary prism which mainly consist of newly formed volcanic rocks and oceanic upper crust. Compared to lower temperature models, the crustal accretionary wedge can grow much thicker, however no significant sedimentary component is present in this wedge. Only a thin subduction channel is formed between the plates which mainly consist of serpentinised mantle peridotite.

At the two highest temperatures we modelled ($\Delta T_P = 200 - 250$ K), the layer of newly formed basaltic crust on top of the original oceanic crust grows extremely thick. Therefore, after a very short timespan of only 2 Myr the oceanic crust reaches the same thickness as the overriding continental crust (i.e. 40 – 50 km). The accretionary wedge has a large size and superposition of newly formed mafic volcanic crust over the continental margin can be observed (see Fig. 12e). After 9 Myr the 'wedge' bears resemblance to an internally deformed collisional orogenic structure, as can be seen from Fig. 12f.

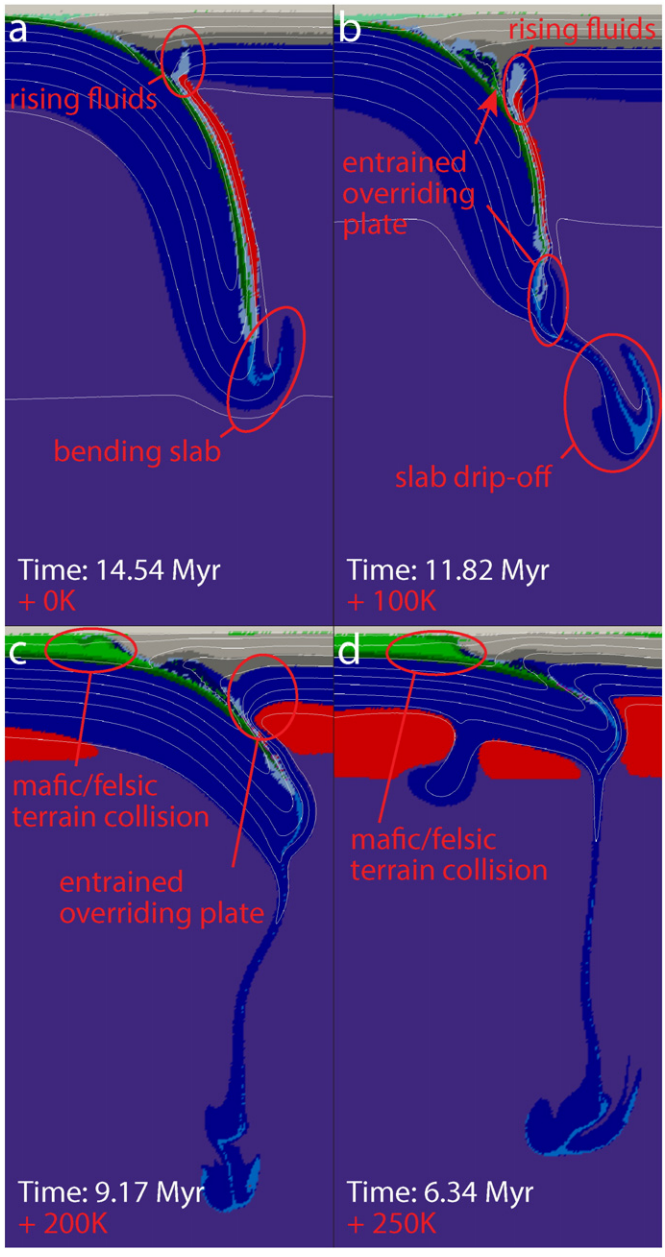

Fig. 10. Variation of the slab geometry with increasing ΔT_P shown in 2D slices of the reference models. Position of the slice corresponds to profile B in Fig. 1.

3.2.4. Variations in geometry and composition of the forearc region

In the present day model *A0* a clearly defined subduction channel forms early in the model development (Fig. 12a). Almost no material from the overriding plate is entrained into the subduction. The overriding plate remains strong and nearly undeformed even close to the trench. A volcanic arc starts to develop at around ~13 Myr and the forearc section is separated from the overriding plate, however it still remains structurally intact (see Figs. 11b and 12b).

At an increased mantle temperature $\Delta T_P = 100$ K delamination of both lithosphere and lower crust of the overriding plate can be observed already at an early stage of subduction (see Figs. 10b, 11c and 12d for details). During this process partially molten and hydrated mantle wedge material ascends from the slab (Fig. 10b). This weakens the structural integrity of the forearc (Fig. 11d). As the slab starts to retreat and partially molten asthenosphere moves into the opening gap between the subducting and overriding plates (Figs. 12d and S2c), the forearc is further weakened and thinned until the collisional stage is reached (Fig. 11d).

For $\Delta T_P = 175$ K the forearc region is weakened by strong flood basalt style volcanism in combination with a growing region of partially molten mantle wedge below the arc (Fig. 7b and c). Due to the fast slab retreat (see also Section 3.2.1) no clear arc is formed and the forearc region is further thinned, weakened and stretched. This pattern continues at higher mantle potential temperatures where the whole forearc region is completely 'reworked' over the course of the model (Figs. 7 and S5).

3.2.5. Variations in arc and backarc region

In all models the upper surface of the plunging slab is hydrated and partially molten (Figs. S1 to S3 and S6). As the slab penetrates deeper into the mantle it continuously drags down hydrated oceanic crust which releases water at depths hydrating overriding mantle wedge peridotite and thus lowering its melting temperature. This well-known fluid-fluxed melting mechanism (Bouilhol et al., 2015, and references therein) allows to partially melt the peridotite atop the slab. Hydrated, partially molten mantle peridotite is positively buoyant compared to the surrounding mantle and with ongoing subduction therefore rises up against the slab motion (Fig. 10a). This upwelling material starts to penetrate and break up the lithosphere of the overriding plate. At this time the first occurrence of new volcanic crust formation can be observed above the upwelling partially molten mantle region which can be interpreted as subduction-related arc volcanism.

In the Phanerozoic model hydrated peridotite with subordinate volume of partially molten hydrated mantle rises from the slab roughly 100 km from the trench in a linear pattern, penetrating the crust in the form of a thin wedge. Only a small amount of newly formed crust is produced forming a narrow but well defined linear arc (Fig. 5c).

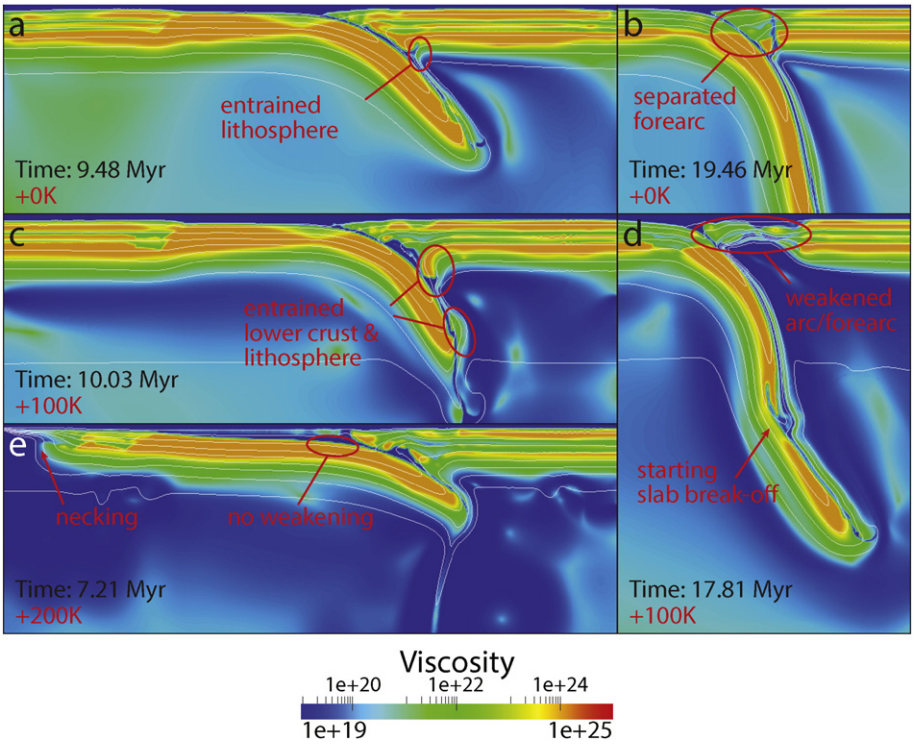

Fig. 11. Variation of the viscosity with increasing ΔT_P shown in 2D slices of the reference models at an earlier ((a), (c), (e)) and later ((b), (d)) stage. Position of the slice corresponds to profile B in Fig. 1.

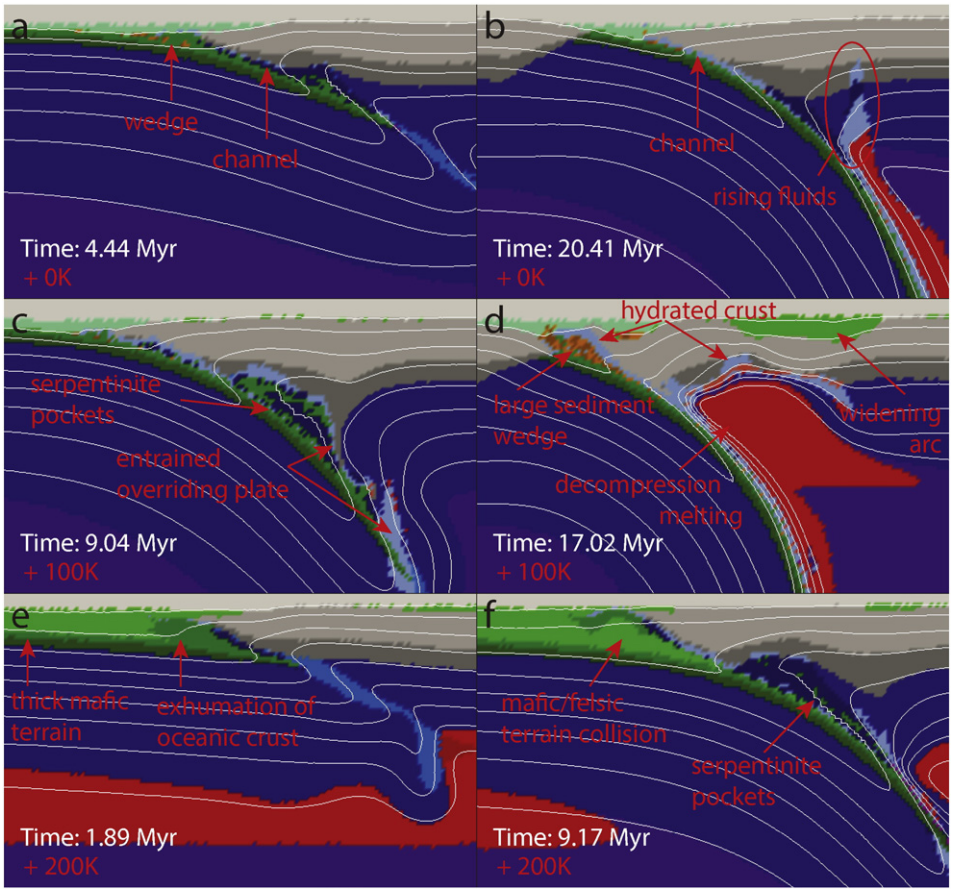

Fig. 12. Variation of the accretionary prism and mantle wedge with increasing ΔT_P is shown in 2D slices of the reference models at an early ((a), (c), (e)) and later ((b), (d), (f)) stage of model development. Position of the slice corresponds to profile B in Fig. 1.

With increasing ΔT_P the amount of partial melt formed from hydrated mantle peridotite increases. Below the young arc a broad partially molten mantle region forms with size and volume largely depending on mantle temperature and which is fed by partially molten hydrated mantle rising from the subducting slab top (see Fig. 6b and c). Slab retreat (see Section 3.2.1) leads to a less clearly defined arc which spreads over a wider region. The backarc region is extended and a backarc-basin formed which is filled by basalts derived from decompression melting of rising asthenosphere. At $\Delta T_P = 100$ K an 80 km wide, relatively shallow arc crust is formed in this manner (Fig. 12d).

For high ΔT_P a large area of partially molten mantle forms below the arc region (Fig. S3a), which produces a rheologically weak gap between the overriding plate and the slab and allows for the formation of large amounts of volcanic rock. With ever increasing temperature the arc grows in width. In model *A5* ($\Delta T_P = 175$ K) no penetration of the crust by rising hydrated and partially molten mantle is observed and new crust is formed over a much wider area but with smaller thickness (Fig. 7c). In model *B4h* ($\Delta T_P = 200$ K, see Table S1 and Figs. S5 and S6) due to the fast slab retreat no pronounced linear arc is formed but the trench is followed directly by a broad region of overriding plate extension and intense distributed basaltic volcanism (Figs. S5c to S5e).

With increasing ΔT_P larger volumes of arc basalts are produced which are spread over a wider area, having a thickness of 8 – 12 km with maximum thickness at $\Delta T_P = 100$ K (Fig. 12b, d and f).

3.2.6. Relationship between fluid-fluxed and decompression mantle melting

There are two different melting mechanisms considered by our models. Fluid-fluxed melting can only occur in hydrated crustal and mantle rocks and predominantly occurs on top of the downgoing slab which acts as a continuous source of water. As seen in Fig. 13b hydrated partial melt first appears at ~10 Myr. Its volume continuously increases but no significant systematic changes with increasing ΔT_P can be observed. Models with $\Delta T_P = 200$ K and 250 K never reach a model age of 10 Myr and no subduction is initiated. Therefore, nearly no hydrated partial melt is formed in these models. A second melting mechanism is dry decompression melting. Decompression melting mainly occurs in sublithospheric zones of upwelling hot mantle and the source material is predominantly dry asthenosphere. From Fig. 13a two maxima of dry melting can be identified (though the second maximum is not reached). The early maximum is related to initial mantle temperature conditions. With increasing ΔT_P the volume of dry partial melt present in the asthenosphere increases since the region where the geotherm crosses the peridotite solidus increases in size. The amount of partially molten dry mantle decreases after formation of the new thick basaltic crust at the surface (Figs. 13a and 14), which increases lithostatic pressure in the asthenosphere and thus decreases the extent of dry decompression melting. From ~12 Myr the dry partial melt volume increases again because in the mantle wedge above the slab a growing area of partially molten mantle is developing due to the overriding lithosphere thinning (see e.g. Fig. 12d). Decompression melting of the mantle wedge cannot be observed for $\Delta T_P = 0$ K and is only a very minor effect at $\Delta T_P = 50$ K. However, with increasing ΔT_P the area of dry decompression melting in the mantle wedge is notably growing and for $\Delta T_P \geq 150$ K decompression melting of sublithospheric mantle also occurs away from the mantle wedge in increasing volumes (Fig. 8c).

In the Phanerozoic model fluid-fluxed melting is dominant and partial melting mainly occurs on top of the downgoing slab. In models with an increased ΔT_P decompression melting mechanisms become increasingly more important. At lower $\Delta T_P = 50 - 150$ K it is still confined to the mantle wedge and leads to the formation of a wider arc as discussed above in Section 3.2.5. For $\Delta T_P = 150 - 250$ K decompression melting occurs along the entire LAB surface and extensive broadly distributed basaltic crustal growth shows characteristic of flood basalt style volcanism.

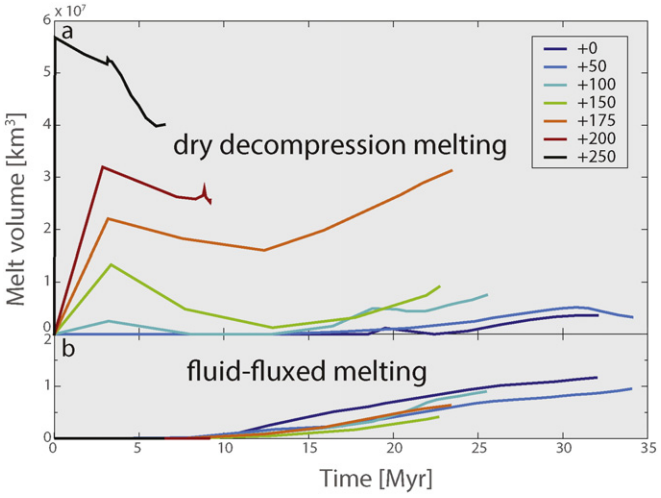

Fig. 13. For all models *A0*–*A6* with $\Delta T_P = 0 - 250$ K in the top panel (a) the total volume of partially molten mantle produced by dry decompression melting is shown (comprised of Figs. S12c, S12j and S12k). (b) In the bottom panel the volume of partially molten mantle produced by fluid-fluxed melting is shown (comprised of Fig. S12l). Partial melt from newly formed crust is not considered. A detailed analysis of volume change by composition for all fluids is given in Fig. S12.

3.2.7. Variations in volume and composition of newly formed crust

With increasing ΔT_P the curves in Fig. 14 show an increasingly higher volume of the newly formed basaltic crust produced from larger volumes of partially molten asthenosphere initially present in the respective models (see Figs. 13a and 14). This broadly distributed basaltic crust growth occurs for all models with $\Delta T_P > 50$ K and is not confined to the subduction-related arc. For high temperature models starting out at a high volume of newly formed volcanic rock in the following quiet period the total amount of new crust is slightly decreasing. This is both due to subduction of newly formed crust (see Fig. 14, dashed lines) and due to the simplified erosion model, which instantaneously removes volcanic rocks deposited above the prescribed erosion level. In Fig. 14 the change in slope at around 12 – 15 Myr marks the onset of arc volcanism where large volumes of crust are produced confined to the relatively small area of the volcanic arc. The difference between solid and dashed line in Fig. 14 indicates the amount of subducted new crust and is growing with increasing ΔT_P. As arc volcanism is confined to the overriding continental plate we can conclude that at high

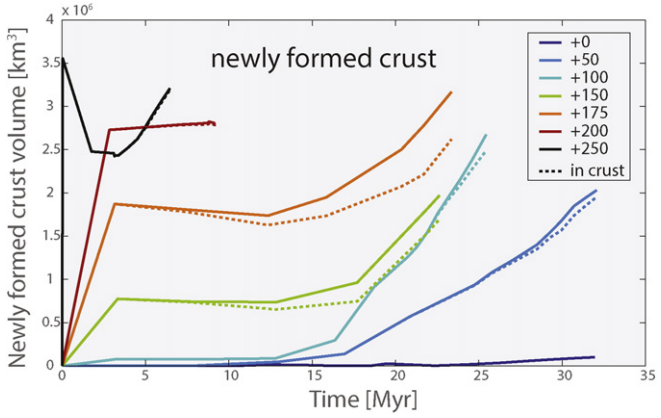

Fig. 14. The total volume of volcanic rock present in the course of the model is shown in solid lines for models *A0*–*A6* with $\Delta T_P = 0 - 250$ K. The volume of volcanic rock without rocks subducted to depths >50 km is shown in dashed lines. Eroded material is not considered. A detailed analysis of volume change by composition for all solids is given in Fig. S11.

ΔT_P not only are large amounts basaltic new crust formed on the oceanic plate and in the trench but also increasing volumes are subducted. The very high temperature models *A*4 and *A*6 with $\Delta T_P = 200$ K and 250 K are again an exception where self-sustained modern-style subduction is never initiated. Arc volcanism or subduction of newly formed crust can therefore not be observed in these models.

3.2.8. Variation in structural behaviour of the crust and mantle lithosphere

In the present day model, the plates move as rigid entity leaving the crust nearly undeformed. However, at increased ΔT_P the compressional setup leads to buckling in the continental crust of the subducting plate and delamination of the overriding crust close to the subduction zone. At $\Delta T_P = 100$ K a slight buckling of the subducting continental crust can be observed which shows its already weakened state (Fig. 15b). At $\Delta T_P = 150$ K the overriding crust is strongly buckled also away from the subduction zone and the lower crust starts to delaminate. Similar behaviour is observed at $\Delta T_P > 150$ K. This behaviour which leads to a deformed and inhomogeneous base of the crust is rheologically mirrored by buckling of the lithosphere producing planar sheet-like or cylindrical drips (Figs. 7b, c and 8c).

Further indication for the increasingly weakened rheological state of the plates are given by the passive margin. The connection between oceanic and continental plate in the subducting plate shows nearly no indication of the applied stress in the present day model (Fig. 15a). With increasing ΔT_P the continental crust in the passive margin zone is thickened due to compression (Fig. 15b). For $\Delta T_P = 150$ K and higher the passive continental margin is typically pushed down into the mantle starting a symmetrical subduction of the oceanic lithosphere from both ends (see Fig. S5).

In several models with an increased $\Delta T_P > 100$ K (in one case *B*2 (see Table S1) even for $\Delta T_P = 100$ K) it can be observed that above a zone of strong mantle upwelling the lithosphere becomes strongly thinned and partially molten until hot partially molten asthenospheric mantle directly reaches the crust (Figs. 7c and 15c). At this point the lower crust starts to melt (Fig. S3c) and the once structurally coherent plate is effectively broken into two fragments. This necking process can be observed in both continental and oceanic plates as well as in the subducting and overriding plate. It preferentially appears on the left or right model boundary but can also be observed inside the model (Figs. 11d and S5).

All of the above described processes lead to an increasingly inhomogeneous base of the lithosphere for higher ΔT_P. For $\Delta T_P \geq 150$ K these inhomogeneities are then able to spawn thermal or thermochemical edge-instabilities which coincide with cold lithospheric mantle downwellings. These downwellings can show characteristics of either cylindrical or planar sheet-like drips (descending cold plumes) (Figs. 7c, 8c and 15c).

3.2.9. Variations in the mantle flow pattern

The general mantle flow pattern as observed in the present day model is very simple. Material flows in through both side boundaries and leaves through the model bottom (Fig. 3a). Through the course of the model this pattern mainly stays the same. The mantle downwelling in the middle of the model box gets more pronounced and focused below the subducting slab. Additionally, during subduction, a poloidal flow around the slab tip can be observed.

Due to the different velocity boundary conditions (see Fig. 3 and Section 2.1.1) model *A*1 ($\Delta T_P = 50$ K) and *A*2 ($\Delta T_P = 100$ K) show slightly different convection patterns than model *A*0. However major features are consistent. The formation of two stable convection cells soon after subduction initiation can be observed. These convection cells remain stable until the collisional stage and break-off of the slab (Fig. 16a). Also the poloidal flow around the slab tip can be observed (Fig. 16a).

For $\Delta T_P > 100$ K however no stable configuration of convection can be established during subduction. The number of convection cells varies

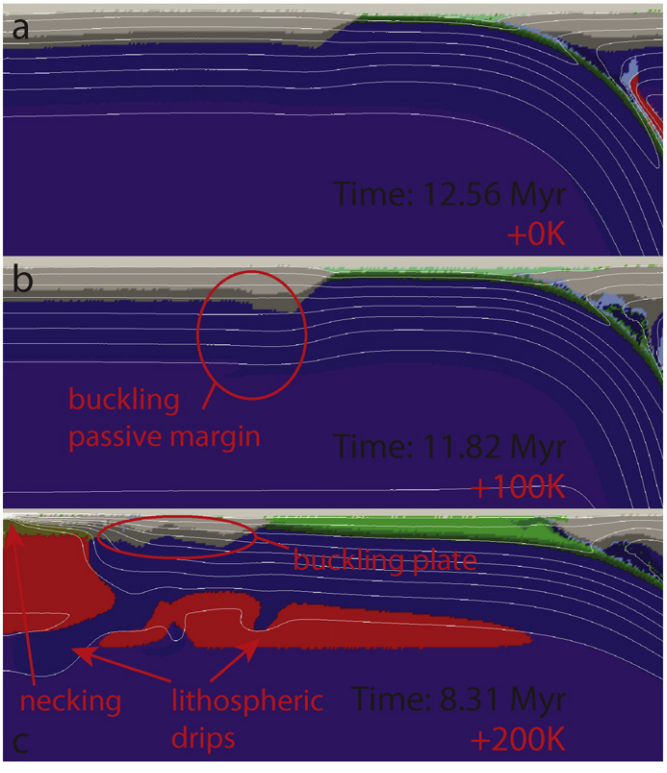

Fig. 15. Evolution of the passive margin with increasing ΔT_P is shown in 2D slices of the reference models. Position of the slice corresponds to profile B in Fig. 1.

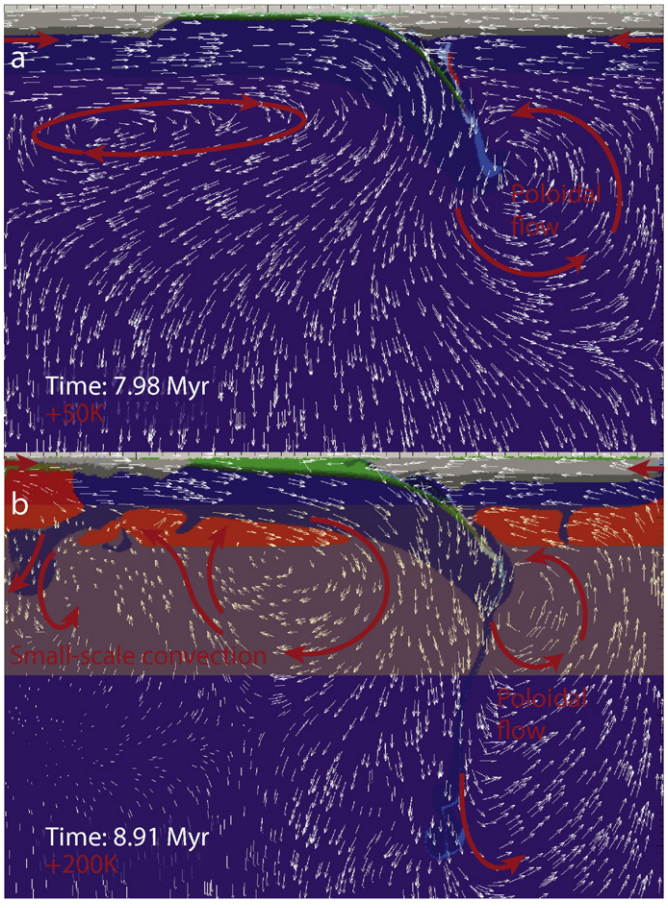

Fig. 16. Mantle flow pattern for (a) model *A*1 ($\Delta T_P = 50$ K) and (b) model *A*4 ($\Delta T_P = 200$ K). For increased ΔT_P an area of small-scale mantle convection forms between 100 − 300 km. Position of the slice corresponds to profile B in Fig. 1.

over the horizontal model extent generally increasing with increasing ΔT_P. This small scale convection is very shallow though and limited to the uppermost ~300 km of the mantle (Fig. 16b).

4. Discussion

4.1. Geodynamic regimes of subduction and lithospheric dynamics in numerical experiments

In the following, the above described models are grouped into four regimes for the purpose of easier description. However, it should be kept in mind that no strict boundaries are observed between these regimes and gradual development from Precambrian plume-lid tectonics (Gerya et al., 2015) to present day subduction and plate tectonics seems more likely.

4.1.1. Regime I: present day subduction $\Delta T_P = 0$ K

The first regime is used as a reference case for present day subduction (see Section 3.1 and Fig. 5) and can nowadays be observed globally in different stages e.g. the Andes or the Himalayas.

4.1.2. Regime II: dripping subduction $\Delta T_P = 50 - 100$ K

The second regime is still very similar to present day subduction and at increased mantle temperatures of 50 − 100 K the large-scale subduction process still operates in the same manner as at the present day mantle temperature (see Fig. 6 for an overview). However, there are clear indications of plates weakened by increased temperature, like buckling of the subducting plate (Fig. 15b), beginning delamination of the lower crust in the overriding plate (Fig. 10b), increasingly earlier drip off from the slab tip (Fig. 18), starting necking of the slab (Fig. 11d) and larger volumes of partially molten asthenosphere (Fig. 13). Drip-off from the subducting slab (see Fig. 6b) can occur repeatedly during the subduction process. With increasing mantle temperature, the first drip-off from the slab tip occurs earlier after subduction initiation (Fig. 18). Due to the short model runtime no slab break-off can be observed (apart from the slab break-off and subsequent opening of a slab window directly below the orogen e.g. in Fig. 5c). However, weakening of the slab at higher temperatures (Fig. 11d) suggests that slab break-off could occur for longer model runtime. This has already been observed by van Hunen and van den Berg (2008) and Moyen and van Hunen (2012).

We call this regime 'dripping subduction' as it is characterised by a stable subduction zone which is still very similar to present day subduction but with multiple drips from the slab tip and possible slab break-off. Van Hunen and van den Berg (2008) and Moyen and van Hunen (2012) found what can be called 'episodic subduction' as they observed multiple slab break-off under similar conditions. We therefore suggest that our observed dripping subduction regime could correspond to episodic subduction at its early stage.

4.1.3. Regime III: transitional mode $\Delta T_P = 150 - 200$ K

In a third regime, active primarily at a mantle potential temperature increase of $\Delta T_P = 150 - 200$ K, the tectonic process shows (see Fig. 7) both features of subduction (Sections 4.1.1 and 4.1.2) as well as plume-lid tectonics (Section 4.1.4). In this transitional mode, the slab tip starts to weaken and neck off very rapidly after the subduction initiation, although not fast enough to terminate the formation of a slab. At $\Delta T_P =$ 200 K (e.g. model *B4h* as shown in Table S1 and Figs. S5 and S6) the subducting slab warms up rapidly and eventually becomes entrained in mantle convection and loses coherency. Additionally, with increasing temperature the subduction becomes ablative (two-sided) (e.g. Davies, 1992) and increasingly large portions of overriding mantle lithosphere and lower continental crust become entrained into the subduction process. This leads to an increasingly two-sided geometry of the subduction zone, though still notably asymmetrical (Figs. 11c, e and S5).

The two stable large-scale convection cells, present at the left and right side of the slab at lower mantle temperature (Fig. 16a), break up into a series of multiple smaller convection cells forming directly below the LAB (Fig. 16b). These convection cells are very non-stationary and are also associated with increasingly laterally inhomogeneous temperature distribution at the base of the lithosphere. Above mantle downwellings thermochemical instabilities form, which produce drips of cold lithosphere into the asthenospheric mantle (Figs. 7c and S5).

4.1.4. Regime IV: plume-lid tectonics $\Delta T_P > 200$ K

For increases in the upper mantle temperature of $\Delta T_P > 200$ K or higher subduction is no longer observed even in our kinematic modern-style subduction setup (see Fig. 8). Instead a new tectonic style emerges which is strongly dominated by up- and downwelling, intensely convecting mantle which interacts with the internally deforming (non-subducting) lithospheric lid. Intense volcanism is no longer constrained to volcanic arcs but forms extensive planes of newly formed mantle derived mafic (basaltic) crust (see Fig. 8c but also Fig. S10). Oceanic and continental crust grow to roughly the same thickness which strongly hinders subduction. Strong mantle return flow leads to melting at the edges of the model and breaks up the lithosphere, thus precluding its plate-like behaviour.

This geodynamic regime, usually named 'plume tectonics', 'plume-lid tectonics' or 'heat-pipe regime', has been previously discussed (Hamilton, 1998; Smithies et al., 2003; Herzberg, 2014) and modelled (Vlaar et al., 1994; François et al., 2014; Johnson et al., 2014; Gerya et al., 2015) by several authors. Van Kranendonk (2011) also proposed a very similar conceptual model to describe the asthenospheric mantle formation of the Barberton Greenstone belt in South Africa as well as the East Pilbara Terrane in Western Australia (Van Kranendonk, 2010) and Hill et al. (1991) discuss a similar model for the Yilgarn Block of Western Australia. Recent studies also show the onset of subduction-like dynamics from plume-lid tectonics (Gerya et al., 2015; Sizova et al., 2015). In this study our aim was to start at the present day end-member, plate tectonics, and find possible tectonic regimes and transitions from plate tectonics to plume-lid tectonics. The present day plate-tectonics-like setup (Figs. 1 and 2) is obviously unsuitable for proper investigation of plume-lid tectonics (Gerya et al., 2015; Sizova et al., 2015; Fischer and Gerya, in press), which is beyond the scope of this study.

4.2. Linking temperature and plate strength

The main parameter which is changed between the various models here is the mantle potential temperature. Increasing the mantle temperature but keeping the surface temperature and lithospheric thickness constant produces notable steepening of the crustal and lithospheric geotherms. This affects various other parameters as well but mainly the lithospheric viscosity profile. As shown in Fig. 17b, below oceanic crust the viscosity drops by around one to two orders of magnitude while the strong part of the plate thins. The same is true below continental crust (Fig. 17a). Due to the mantle viscosity decrease at increased mantle temperature the base of the lithosphere starts to build drips and folds more easily. Additionally, the continental strength is lowered and the connection between crust and subcrustal mantle-lithosphere as well as between upper and lower crust is weakened. This allows for easier delamination of continental crust at increased upper-mantle temperature. This effect can mainly be observed at the subduction trench where at higher temperatures also upper continental crust is entrained in the ablative subduction process (see e.g. Fig. 12c).

4.3. Consequences of wide-spread mantle-derived magmatism

New basaltic crust formed on top of oceanic crust does not destabilise the layering. The dynamics can however be influenced due to the fact that the oceanic crust effectively becomes thicker and thus more positively buoyant. This thicker oceanic crust influences dynamics

in two ways. The added thickness allows for a larger accretionary wedge to be built which hinders subduction and chokes the subduction zone. The resulting dynamics resemble a collisional process (see e.g. Fig. 12f) which can be found in modern continent-continent collision or island arc accretion zones.

Volcanic crust of basaltic composition however is denser than upper continental crust and thus newly formed crust formed on top of continental crust is gravitationally unstable. Large amounts of volcanic rocks erupting in a flood basalt style on top of a weakened continental crust lead to an overturn in the crust (François et al., 2014; Johnson et al., 2014). Denser mafic crust starts to sink down into the underlying felsic crust which in turn starts to dome up (e.g. Figs. 8c and 12d). This tendency seems similar to the beginning of the development of a typical dome-and-keel structure (Van Kranendonk, 2011), although longer-term 3D models with hot mantle temperature will be needed for properly investigating crustal doming processes triggered by mantle-derived magmatism (Fischer and Gerya, in press).

The strong volcanism and large volume of crust formation leave behind a growing layer of depleted asthenospheric mantle effectively cooling it down and turning it into a depleted lithosphere. However, this rudimentary lithosphere is not stable under high T_P conditions and frequently drips off into the mantle. This generates a return flow and more decompression melting which in turn generates more new crust and depleted mantle (Johnson et al., 2014).

4.4. Formation of small plates

Thinning and necking of the lithosphere and crust can mainly be observed at model boundaries. Thinning of the plate (as e.g. seen in Figs. 15c and S3c) is caused by hot mantle upwelling. The process therefore occurs more often and faster at higher mantle potential temperature. At higher ΔT_P smaller scale convection cells directly below the lithosphere can also lead to thinning of the former, e.g. above the mantle wedge (Figs. S2c and S6e). With the given boundary conditions (Fig. 3b) and model box size and ratio, mantle convection is forced to form upwellings at the left and right model boundaries. Considering these limitations, these findings seem to indicate formation of smaller plates with higher ΔT_P (Sizova et al., 2010).

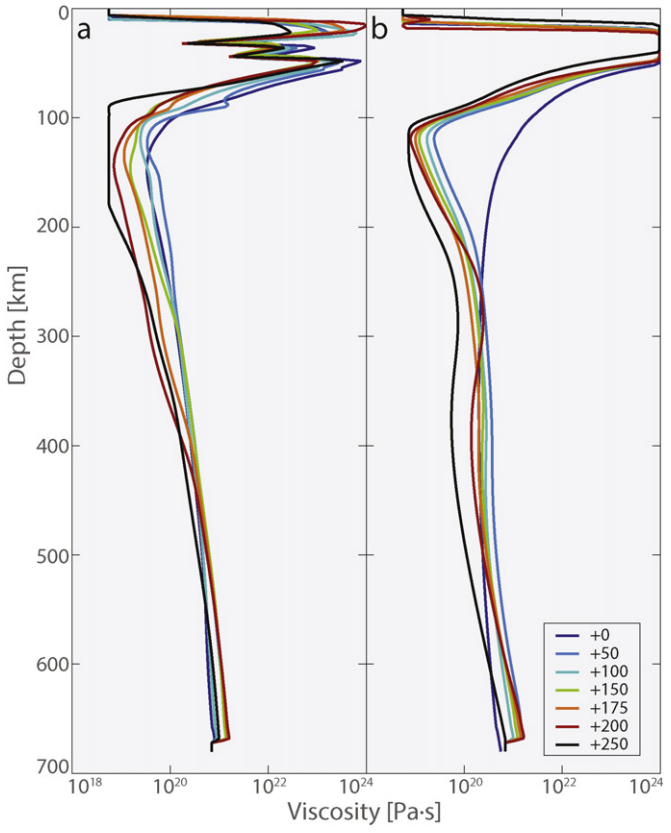

Fig. 17. Effective (visco-plastic) viscosity profiles for both (a) continental and (b) oceanic lithosphere at $\Delta T_P = 0 - 250$ K corresponding to reference models A0 to A6. Position of the profiles corresponds to localities D (oceanic) and E (continental) in Fig. 1.

4.5. Slab break-off and initiation of cold plumes

Fig. 18 shows the timing of the first slab break off or necking with different ΔT_P. At present day mantle temperature, the slab only breaks off after continental collision. For an increased ΔT_P an earlier drip off at a shallower depth indicates the start of dripping subduction. At $\Delta T_P \geq 200$ K the subducting plate drips off within <4 Myr or as soon as it enters the mantle and modern-style subduction is thus no longer possible. For an increase in $\Delta T_P = 100$ K the slab viscosity is lowered by roughly an order of magnitude (van Hunen and Moyen, 2012). Van Hunen and Allen (2011) showed that a weakened slab leads to a shorter delay time between continental collision following slab break off. The process of slab necking and tearing is also sped up within a weakened slab (van Hunen and Allen, 2011). Furthermore, van Hunen and van den Berg (2008) showed that for increasing ΔT_P subduction becomes faster and more episodic.

At $\Delta T_P = 150$ K cold plumes or Rayleigh–Taylor instabilities appear for the first time not at the slab tip but at the base of the lithosphere (Fig. 18). With further increasing ΔT_P the number of "off-slab" RT-instabilities appearing during the course of the model increases while the onset time decreases.

4.6. Factors inhibiting the subduction process

Several factors can either hinder or totally inhibit subduction. With increasing ΔT_P more lithospheric material of the overriding plate is entrained which eventually leads to a more two-sided (ablative) subduction style (Davies, 1992). Rheological weakening of the continental crust also leads to delamination of the lower crust which can slow down subduction substantially because of the low density of the continental crust. In addition, oceanic crust on the subducting plate is growing thicker and its positive buoyancy is increased which could further hinder subduction in the beginning before eclogitisation depth is reached (van Hunen and van den Berg, 2008).

Very strong crustal growth of the oceanic crust by mantle-derived magmatism can also lead to a growing size of the accretionary prism. The subduction zone becomes locked as increasingly larger volumes of the newly-formed volcanic rocks are accreted into what starts to

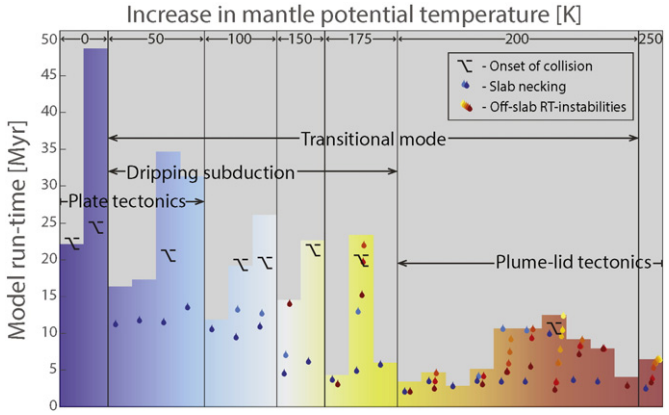

Fig. 18. Important events during the model evolution are shortly summarised for all models in Table S1. The length of the bar indicates the maximum length of the model run t_{max}. The black symbol at ~20 Myr indicates continental collision. Blue drips signify necking or dripping restricted to the slab tip, whereas yellow/red drips signify dripping away from the slab.

resemble a collisional orogen between a felsic and a mafic terrain (Fig. 12f and Davies (1992)).

The higher mantle temperature and subsequent weakening of a subducting slab leads to an earlier slab break-off. The major driving force of subduction (van Hunen and Moyen, 2012) is therefore effectively removed. Especially at $\Delta T_P \geq 200$ K subduction is practically impossible to start as any lithospheric discontinuity simply drips off immediately (Fig. 8c and Davies (1992); Smithies et al. (2003)).

4.7. The onset of subduction

One of the most strongly debated questions about early Earth tectonics is how and when did the first subduction zone initiate. To answer these questions, we need to consider secular changes in global geodynamic regimes forward in time. As suggested for example by Van Kranendonk (2011) for the South African Kaapvaal craton and by François et al. (2014) for the Australian East Pilbara craton the dominating tectonic regime in the earlier Archean was plume-lid tectonics, which consists of a stable two-layer convection-system with separate crustal doming and mantle convection with a strong emphasis on vertical movement (Vlaar et al., 1994; Smithies et al., 2003; Van Kranendonk, 2011; François et al., 2014). A sketch of Archean Plume-lid tectonics as modelled by Fischer and Gerya (in press) is shown in Fig. 19.

With decreasing ΔT_P the lithosphere and crust strengthens and more material becomes entrained by lithospheric dripping. This dripping process might indeed help to initiate horizontal motions in the crust as well. Further decrease in ΔT_P will lead to a dripping which eventually is able to entrain lower crustal material as well. At this stage, dripping therefore starts to resemble a two-sided subduction (Fig. S5c and Davies (1992)). However, this very early proto-subduction will remain episodic and associate with frequent slab necking and dripping. With further cooling of the mantle colder, stronger, more coherent and longer slabs become feasible. Further decrease in ΔT_P allows to strengthen the slab and leads to less frequent slab break-off and finally a stable subduction process (van Hunen and van den Berg, 2008; Gerya et al., 2015).

The described evolutionary progression corresponds to a gradual transition between the two end-members plume-lid tectonics in the early Archean and Subduction in the Phanerozoic. Therefore, any time between the Archean and the Present may show some kind of subduction-like dynamics. However how close to present day the transition to modern-style subduction and plate tectonics was, remains debatable. Our models thus, suggest gradual rather than abrupt plume-lid tectonics to plate tectonics transition in the Earth's history.

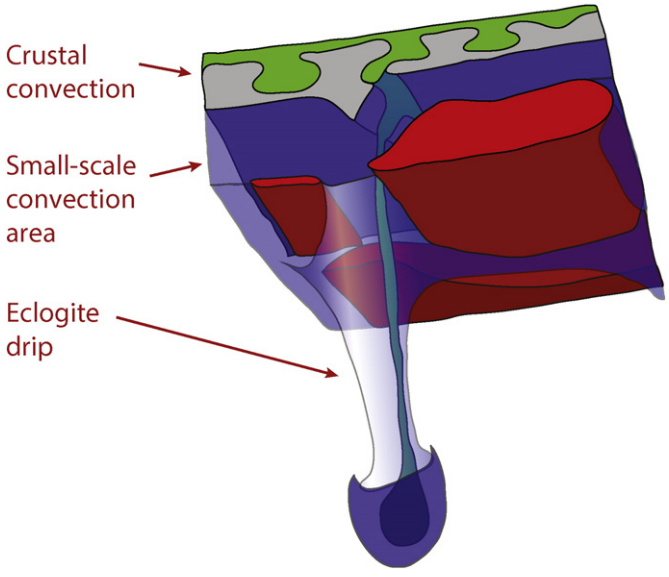

Fig. 19. Sketch of Precambrian tectonics. The crust is dominated by diapiric overturns. Cold overthickened unstable lithosphere drips down into the mantle initiating delamination or two-sided subduction.

4.8. Setup dependencies and model limitations

Knowledge about the global geodynamic style and lithospheric and crustal conditions during the Precambrian are very limited and the explored modern-style plate tectonic setup may, therefore, be not fully appropriate for analysing the Precambrian mantle and crustal dynamics. Due to a model setup and kinematic boundary conditions which are very similar to present day, subduction can be observed up to very high temperatures. Still subduction stability clearly breaks at roughly $\Delta T_P = 200$ K compared to present-day mantle potential temperature. Presumably, without kinematically prescribed plate motions subduction might destabilise at even lower temperatures but this requires careful investigation based on self-consistent models with spontaneously moving plates (e.g. Sizova et al., 2014).

At increased ΔT_P the influence of the erosion level becomes more visible. Erosion level is chosen either 8 or 4 km above the water level and continent surface which seems to inhibit formation of larger volumes of volcanic crust by instantaneous erosion in some cases. Since sedimentation in our models is in fact independent of erosion (see Section 2.1.1) nearly no sedimentation occurs in response to the instantaneous erosional mass removal. Consequently, implementation of more sophisticated erosion/sedimentation treatment approaches is desirable in the future. Last but not least, crustal growth in our models is assumed to be fully controlled by surface volcanism, whereas on Earth intrusive crustal accretion in form of plutons is dominant, which calls for the use of more realistic melt emplacement algorithms (e.g. Vogt et al., 2012).

5. Conclusion

We varied the mantle potential temperature T_P in a 3D present day subduction model up to $\Delta T_P = 250$ K. In models with $\Delta T_P = 200 - 250$ K we found that subduction is no longer possible and model evolution is driven by intense tectono-magmatic plume-lithosphere interactions instead. We therefore propose that the early Archean Earth was radically different and was driven by plume-lid tectonics. Its major elements are a thick crust of 35 − 50 km which is internally convecting and an unstable lithosphere which displays vigorous small-scale instabilities and thinning by dripping. Due to strong small-scale convection larger plates are also often broken up into smaller fragments. At a lower $\Delta T_P = 150 - 200$ K models are subjected to frequent necking and dripping processes and show characteristics of both types of tectonics: Present day subduction and plume-lid tectonics. For $\Delta T_P < 150$ K signs of plume-lid tectonics disappear. At slightly elevated temperatures of $\Delta T_P = 50 - 150$ K subduction has dripping and (possibly) episodic character and shows signs of weakened plates.

We conclude that tectonics, starting out from plume-lid tectonics, evolved gradually into what we can observe today as plate tectonics and subduction. Therefore, most likely no abrupt geodynamic regime transition point can be specified as subduction gradually evolved over time.

Acknowledgments

This study was co-funded by an ETH-grant ETH-37_11-2, by an ERC ITN-grant ZIP (T.G.), by a SNF-project Swiss-AlpArray (T.G.), by a SNF-grant 200021_149252. Simulations were performed on the ETH-Zurich Brutus cluster. Constructive reviews of Jeroen van Hunen and an anonymous reviewer are appreciated. Daniel Bower is thanked for proofreading of the manuscript.

Appendix A. Supplementary data

Supplementary data to this article can be found online at http://dx.doi.org/10.1016/j.gr.2016.06.002.

References

Abbott, D., Burgess, L., Longhi, J., Smith, W.H.F., 1994. An empirical thermal history of the Earth's upper mantle. Journal of Geophysical Research: Solid Earth 99 (B7), 13835–13850.

Bittner, D., Schmeling, H., 1995. Numerical modelling of melting processes and induced diapirism in the lower crust. Geophysical Journal International 123 (1), 59–70.

Bleeker, W., Ketchum, J.W., Jackson, V.A., Villeneuve, M.E., 1999. The central slave basement complex, part I: its structural topology and autochthonous cover. Canadian Journal of Earth Sciences 36 (7), 1083–1109.

Bouilhol, P., Magni, V., van Hunen, J., Kaislaniemi, L., 2015. A numerical approach to melting in warm subduction zones. Earth and Planetary Science Letters 411, 37–44.

Burg, J.P., Gerya, T.V., 2005. The role of viscous heating in Barrovian metamorphism of collisional orogens: thermomechanical models and application to the Lepontine dome in the Central Alps. Journal of Metamorphic Geology 23 (2), 75–95.

Canup, R.M., 2004. Origin of terrestrial planets and the earth–moon system. Physics Today 57 (4), 56–62.

Chardon, D., Gapais, D., Cagnard, F., 2009. Flow of ultra-hot orogens: a view from the Precambrian, clues for the Phanerozoic. Tectonophysics 477 (3–4), 5–118.

Clauser, C., Huenges, E., 1995. Thermal Conductivity of Rocks and Minerals. In: Ahrens, T. (Ed.) Rock Physics and Phase Relations Vol. 3. AGU Reference Shelf, pp. 105–126.

Collins, W., Kranendonk, V.,.M.J., Teyssier, C., 1998. Partial convective overturn of Archaean crust in the east Pilbara Craton, Western Australia: driving mechanisms and tectonic implications. Journal of Structural Geology 20 (9), 1405–1424.

Connolly, J.A.D., 2005. Computation of phase equilibria by linear programming: a tool for geodynamic modeling and its application to subduction zone decarbonation. Earth and Planetary Science Letters 236 (1–2), 524–541.

Crameri, F., Schmeling, H., Golabek, G.J., Duretz, T., Orendt, R., Buiter, S.J.H., May, D.A., Kaus, B.J.P., Gerya, T.V., Tackley, P.J., 2012. A comparison of numerical surface topography calculations in geodynamic modelling: an evaluation of the sticky air' method. Geophysical Journal International 189 (1), 38–54.

Crisp, J.A., 1984. Rates of magma emplacement and volcanic output. Journal of Volcanology and Geothermal Research 20 (3–4), 177–211.

Davies, G.F., 1992. On the emergence of plate tectonics. Geology 20 (11), 963–966.

de Wit, M.J., 1998. On Archean granites, greenstones, cratons and tectonics: does the evidence demand a verdict? Precambrian Research 91 (1), 181–226.

Duretz, T., Gerya, T.V., Spakman, W., 2014. Slab detachment in laterally varying subduction zones: 3-D numerical modeling. Geophysical Research Letters 41 (6), 1951–1956.

Fischer, R., Gerya, T., 2016. Early earth plume-lid tectonics: a high-resolution 3D numerical modelling approach. Journal of Geodynamics (in press).

François, C., Philippot, P., Rey, P., Rubatto, D., 2014. Burial and exhumation during Archean sagduction in the east Pilbara granite-greenstone Terrane. Earth and Planetary Science Letters 396 (0), 235–251.

Furnes, H., Dilek, Y., de Wit, M., 2015. Precambrian greenstone sequences represent different ophiolite types. Gondwana Research 27 (2), 649–685.

Gerya, T., 2014. Precambrian geodynamics: concepts and models. Gondwana Research 25 (2), 442–463.

Gerya, T.V., Connolly, J.A.D., Yuen, D.A., Gorczyk, W., Capel, A.M., 2006. Seismic implications of mantle wedge plumes. Physics of the Earth and Planetary Interiors 156 (1–2), 59–74.

Gerya, T.V., Meilick, F.I., 2011. Geodynamic regimes of subduction under an active margin: effects of rheological weakening by fluids and melts. Journal of Metamorphic Geology 29 (1), 7–31.

Gerya, T.V., Stern, R.J., Baes, M., Sobolev, S.V., Whattam, S.A., 2015. Plate tectonics on the earth triggered by plume-induced subduction initiation. Nature 527 (7577), 221–225.

Gerya, T.V., Yuen, D.A., 2003. Characteristics-based marker-in-cell method with conservative finite-differences schemes for modeling geological flows with strongly variable transport properties. Physics of the Earth and Planetary Interiors 140 (4), 293–318.

Gerya, T.V., Yuen, D.A., 2007. Robust characteristics method for modelling multiphase visco-elasto-plastic thermo-mechanical problems. Physics of the Earth and Planetary Interiors 163 (1–4), 83–105.

Govers, R., Wortel, M.J.R., 2005. Lithosphere tearing at STEP faults: response to edges of subduction zones. Earth and Planetary Science Letters 236 (1–2), 505–523.

Hamilton, W.B., 1998. Archean magmatism and deformation were not products of plate tectonics. Precambrian Research 91 (1), 143–179.

Herzberg, C., 2014. Early earth: Archaean drips. Nature Geoscience 7 (1), 7–8.

Herzberg, C., Asimow, P.D., Arndt, N., Niu, Y., Lesher, C.M., Fitton, J.G., Cheadle, J., Saunders, A.D., 2007. Temperatures in ambient mantle and plumes: constraints from basalts, picrites, and komatiites. Geochemistry, Geophysics, Geosystems 8 (2) (n/a–n/a).

Herzberg, C., Condie, K., Korenaga, J., 2010. Thermal history of the earth and its petrological expression. Earth and Planetary Science Letters 292 (1–2), 79–88.

Hess, P., 1989. Origins of Igneous Rocks. Harvard University Press.

Hickman, A., 2004. Two contrasting granite-greenstone terranes in the Pilbara Craton, Australia: evidence for vertical and horizontal tectonic regimes prior to 2900Ma. Precambrian Research 131 (3), 153–172.

Hill, R.I., Campbell, I.H., Griffiths, R.W., 1991. Plume tectonics and the development of stable continental crust. Exploration Geophysics 22 (1), 185–188.

Ito, K., Kennedy, G.C., 1971. An experimental study of the basalt-garnet granulite–eclogite transition. The Structure and Physical Properties of the Earth's Crust. American Geophysical Union, pp. 303–314.

Jaupart, C., Labrosse, S., Mareschal, J.C., 2007. 7.06 — Temperatures, Heat and Energy in the Mantle of the Earth. In: Schubert, G. (Ed.), Treatise on Geophysics. Elsevier, Amsterdam, pp. 253–303 (Ch. 7).

Johannes, W., 1985. The Significance of Experimental Studies for the Formation of Migmatites. Migmatites. Springer US, pp. 36–85 (Ch. 2).

Johnson, T.E., Brown, M., Kaus, B.J.P., VanTongeren, J.A., 2014. Delamination and recycling of Archaean crust caused by gravitational instabilities. Nature Geoscience 7 (1), 47–52.

Katayama, I., Karato, S.-i., 2008. Low-temperature, high-stress deformation of olivine under water-saturated conditions. Physics of the Earth and Planetary Interiors 168 (3–4), 125–133.

Katz, R.F., Spiegelman, M., Langmuir, C.H., 2003. A new parameterization of hydrous mantle melting. Geochemistry, Geophysics, Geosystems 4 (9), 1073.

Keller, T., Tackley, P.J., 2009. Towards self-consistent modeling of the martian dichotomy: the influence of one-ridge convection on crustal thickness distribution. Icarus 202 (2), 429–443.

Kisters, A.F.M., Anhaeusser, C.R., 1995. Emplacement features of Archaean TTG plutons along the southern margin of the Barberton greenstone belt, South Africa. Precambrian Research 75 (1–2), 1–15.

Labrosse, S., Jaupart, C., 2007. Thermal evolution of the earth: secular changes and fluctuations of plate characteristics. Earth and Planetary Science Letters 260 (3–4), 465–481.

McKenzie, D., Bickle, M.J., 1988. The volume and composition of melt generated by extension of the lithosphere. Journal of Petrology 29 (3), 625–679.

Moyen, J.-F., van Hunen, J., 2012. Short-term episodicity of Archaean plate tectonics. Geology 40 (5), 451–454.

Perchuk, L.L., Gerya, T.V., 2011. Formation and evolution of Precambrian granulite terranes: a gravitational redistribution model. Memoir — Geological Society of America 207, 289–310.

Poli, S., Schmidt, M.W., 2002. Petrology of subducted slabs. Annual Review of Earth and Planetary Sciences 30 (1), 207–235.

Ranalli, G., 1995. Rheology of the Earth. Springer.

Schmidt, M.W., Poli, S., 1998. Experimentally based water budgets for dehydrating slabs and consequences for arc magma generation. Earth and Planetary Science Letters 163 (1–4), 361–379.

Schutt, D.L., Lesher, C.E., 2006. Effects of melt depletion on the density and seismic velocity of garnet and spinel lherzolite. Journal of Geophysical Research: Solid Earth 111 (B5), B05401.

Sizova, E., Gerya, T., Brown, M., 2014. Contrasting styles of Phanerozoic and Precambrian continental collision. Gondwana Research 25 (2), 522–545.

Sizova, E., Gerya, T., Brown, M., Perchuk, L.L., 2010. Subduction styles in the Precambrian: insight from numerical experiments. Lithos 116 (3–4), 209–229.

Sizova, E., Gerya, T., Stu¨we, K., Brown, M., 2015. Generation of felsic crust in the Archean: a geodynamic modeling perspective. Precambrian Research 271, 198–224.

Smithies, R.H., Champion, D.C., Cassidy, K.F., 2003. Formation of Earth's early Archaean continental crust. Precambrian Research 127 (1–3), 89–101.

Turcotte, D., Schubert, G., 2002. Geodynamics. second ed. Cambridge University Press.

van Hunen, J., Allen, M.B., 2011. Continental collision and slab break-off: a comparison of 3-D numerical models with observations. Earth and Planetary Science Letters 302 (1–2), 27–37.

van Hunen, J., Moyen, J.-F., 2012. Archean subduction: fact or fiction? Annual Review of Earth and Planetary Sciences 40 (1), 195–219.

van Hunen, J., van den Berg, A.P., 2008. Plate tectonics on the early earth: limitations imposed by strength and buoyancy of subducted lithosphere. Lithos 103 (1–2), 217–235.

Van Kranendonk, M.J., 2010. Two types of Archean continental crust: plume and plate tectonics on early earth. American Journal of Science 310 (10), 1187–1209.

Van Kranendonk, M.J., 2011. Cool greenstone drips and the role of partial convective overturn in Barberton greenstone belt evolution. Journal of African Earth Sciences 60 (5), 346–352.

Van Kranendonk, M.J., Collins, W., Hickman, A., Pawley, M.J., 2004. Critical tests of vertical vs. horizontal tectonic models for the Archaean east Pilbara granite–greenstone terrane, Pilbara craton, western Australia. Precambrian Research 131 (3), 173–211.

Vlaar, N.J., van Keken, P.E., van den Berg, A.P., 1994. Cooling of the earth in the Archaean: consequences of pressure-release melting in a hotter mantle. Earth and Planetary Science Letters 121 (1), 1–18.

Vogt, K., Gerya, T.V., Castro, A., 2012. Crustal growth at active continental margins: numerical modeling. Physics of the Earth and Planetary Interiors 192–193 (0), 1–20.

Wasserburg, G.J., Gordon, J.F.M., Hoyle, F., Fowler, W.A., 1964. Relative contributions of uranium, thorium, and potassium to heat production in the earth. Science 143 (3605), 465–467.

Zhu, G., Gerya, T.V., Tackley, P.J., Kissling, E., 2013. Four-dimensional numerical modeling of crustal growth at active continental margins. Journal of Geophysical Research: Solid Earth 118 (9), 4682–4698.